STUDY OF THE FERMI SURFACES OF

GRAPHITE INTERCALATION COMPOUNDS USING

SHUBNIKOV DE HAAS EFFECT

by

FARHAD HAKIMI

B.S., Massachusetts Institute of Technology
(1976)

SUBMITTED IN PARTIAL FULFILLMENT OF THE

REQUIREMENTS FOR THE DEGREE OF

MASTER OF SCIENCE

at the

MASSACHUSETTS INSTITUTE OF TECHNOLOGY

January, 1980

Signature redacted

Signature of Author..
Department of Electrical Engineering and Computer Science,
December 7, 1979

Signature redacted

Certified by...
Thesis Supervisor

Signature redacted

Accepted by...
Chairman, Departmental Committee on Graduate Students

STUDY OF THE FERMI SURFACES OF

GRAPHITE INTERCALATION COMPOUNDS USING

SHUBNIKOV DE HAAS EFFECT

by

FARHAD HAKIMI

Submitted to the Department of Electrical Engineering and Computer Science on December 7, 1979 in partial fulfillment of the requirements for the Degree of Master of Science.

ABSTRACT

Measurements of the electrical resistivity (ρ) and derivative of electrical resistivity with respect to magnetic field ($\partial\rho/\partial H$) as a function of magnetic field is done on samples of graphite intercalation compounds where the focus has been on the oscillatory behavior with the field (Shubnikov-de Haas effect) rather than the background values of (ρ) and ($\partial\rho/\partial H$). The materials which have been studied are $C_x FeCl_3$ (stage-1, 3, and 7), $C_x pdcl_2$ (stage-3), $C_x Br_2$ (stage-15), $C_x Rb$ (stage-3), and $C_x Alcl_3$ (stage-4).

Possible shapes of the Fermi Surfaces for graphite intercalation compounds has been inferred from angular dependence of Shubnikov-de Haas oscillations. Possible shapes of Fermi Surfaces are sliced ellipsoids formed by zone folding of a graphite like constant energy surface along the c-axis, with possible warping similar to that of pure graphite. It has been found that the larger the cross section of the ellipsoidal Fermi Surfaces, the higher the anisotropy.

Thesis Supervisor: Mildred S. Dresselhaus

Title: Professor of Electrical Engineering and Computer Science

ACKNOWLEDGEMENTS

TABLE OF CONTENTS

LIST OF FIGURES

LIST OF TABLES

CHAPTER 1

INTRODUCTION

Graphite intercalation compounds consist of an alternating sequence of intercalate monolayers separated by n contingous graphite layers ($n \geq 1$) where n denotes the stage of the compound. The chemical reaction by which the compounds are formed is facilitated by the highly anisotropic bonding in graphite; the hexagonal array within a single carbon layer contains very strong sp^2 covalent bonds, whereas adjacent layers are bonded mainly by the weak p_z overlap between nearest-neighbor layers. As a result, the in-plane graphite structure is essentially unchanged by intercalation, while the c-axis spacing can increase by as much as a factor of 3 or more to accommodate the intercalate. Graphite can form synthetic metals by virtue of its aromatic electron band structure. The macro-aromatic molecules in its crystals readily suffers injection or emission of electrons when brought in contact with electron donor or electron acceptor intercalants. Therefore, in principle, metallic solids with wide diversity of electronic characteristics can be synthesized by intercalation of suitable species between sheets of hexagonally bonded carbon atoms in graphite. Two main categories of elements and compounds have been reported to intercalate graphite: donors - esentially Group I and II metals; or acceptors such as halogen molecules Br_2, Icl, ...;

compounds sbd_5, AsF_5, ..., Brönsted acids HNO_3, H_2SO_4, ..., and certain oxides, sulfides and flourides. Interest in these materials stems from the fact that the anisotropy can be varied over a wide range by proper choice of the intercalating species. One of the property changes accompanying intercalation is the large increase in a-axis (in-plane) conductivity σ_a. The anisotropy (σ_a/σ_c) increases with intercalation up to a factor 10^6 for acceptors, while it decreases for alkali metals. This suggests that p-type compounds are strongly two-dimensional. Thus, one can study phenomena peculiar to two dimensional systems in a systematic way. Several practical applications are also expected. Some acceptor compounds have an in-plane conductivity σ_a greater than that of copper with only 1/3 the density. Alkali donor compounds exhibit superconductivity where neither species alone undergoes a superconducting transition. Applications in catalysis is expected where the chemical reactivity of the intercalated molecule is selectively modified by the electron transfer from or to graphite.

Experiments such as, conductivity and specific heat confirm the metallic character of these compounds. The electronic structure of these compounds is still unknown (except for C_8K and C_6Li), in spite of a considerable amount of published experimental results relevant to the electronic structure.

The motivation for the present research is to study the Fermi surfaces of the graphite intercalation compounds in order to obtain insight into the electronic structure of these compounds. The

Shubnikov-de Haas effect has been used to investigate the electronic structure of graphite intercalation compounds. In a high magnetic field and at low temperature, the free electron gas is quantized in Landau levels. The magnetoresistivity oscillates as the magnetic field changes. These oscillations are periodic in inverse field (1/H) and the frequency of the oscillations is given by $F = \frac{\hbar cA}{2\pi e}$ where A is an extremal sectional Fermi surface area perpendicular to the magnetic field. Therefore, by looking at the angular dependence of each frequency, one is able to determine the shape of the Fermi surfaces.

The compounds studied are $C_x FeCl_3$ (stage 1-3-7), $C_x PdCl_2$ (stage 3), $C_x Br_2$ (stage 15), $C_x AlCl_3$ (stage 4), as acceptor compounds and $C_x Rb$ (stage 3) as donor compounds. The effort was focused on the shape of the Fermi surfaces of these compounds, the stage dependence of the frequencies in the $C_x FeCl_3$ system, and the intercalant dependence of these frequencies.

CHAPTER 2

BACKGROUND

In this chapter, we review the graphite energy band structure
which is described by the Slonczewski-Weiss McClure mode. We describe
a model for dilute graphite intercalation compounds based on
modification of the pure graphite structure (M.S. Dresselhaus,
G.F. Dresselhaus, J.E. Fisher, 1977). In Section 2.3, a possible model
for the Fermi surfaces of graphite intercalation compounds has been
introduced. Finally, in Section 2.4, we discuss the Shubnikov de-Haas
effect.

2.1. Energy Band Structure of Graphite

The graphite crystal lattice is shown in figure 2.1. The distance
between layer planes is much larger than the distance between atoms
in a layer, and each atom has three equivalent neighbors in the
same layer. The planes are stacked in ABAB order and there are two
kinds of atomic sites: type A which has neighbors directly opposite
in adjacent planes, and type B which does not. There are four atoms
in a unit cell, an A and B atom from each plane. The Brillouin zone
is a thin hexagonal cylinder as shown in figure 2.2. The Fermi
surfaces are located in the region of the vertical zone edges HKH.

Because of the large anisotropy of the crystal structure, it
is a reasonable starting approximation to ignore the interaction
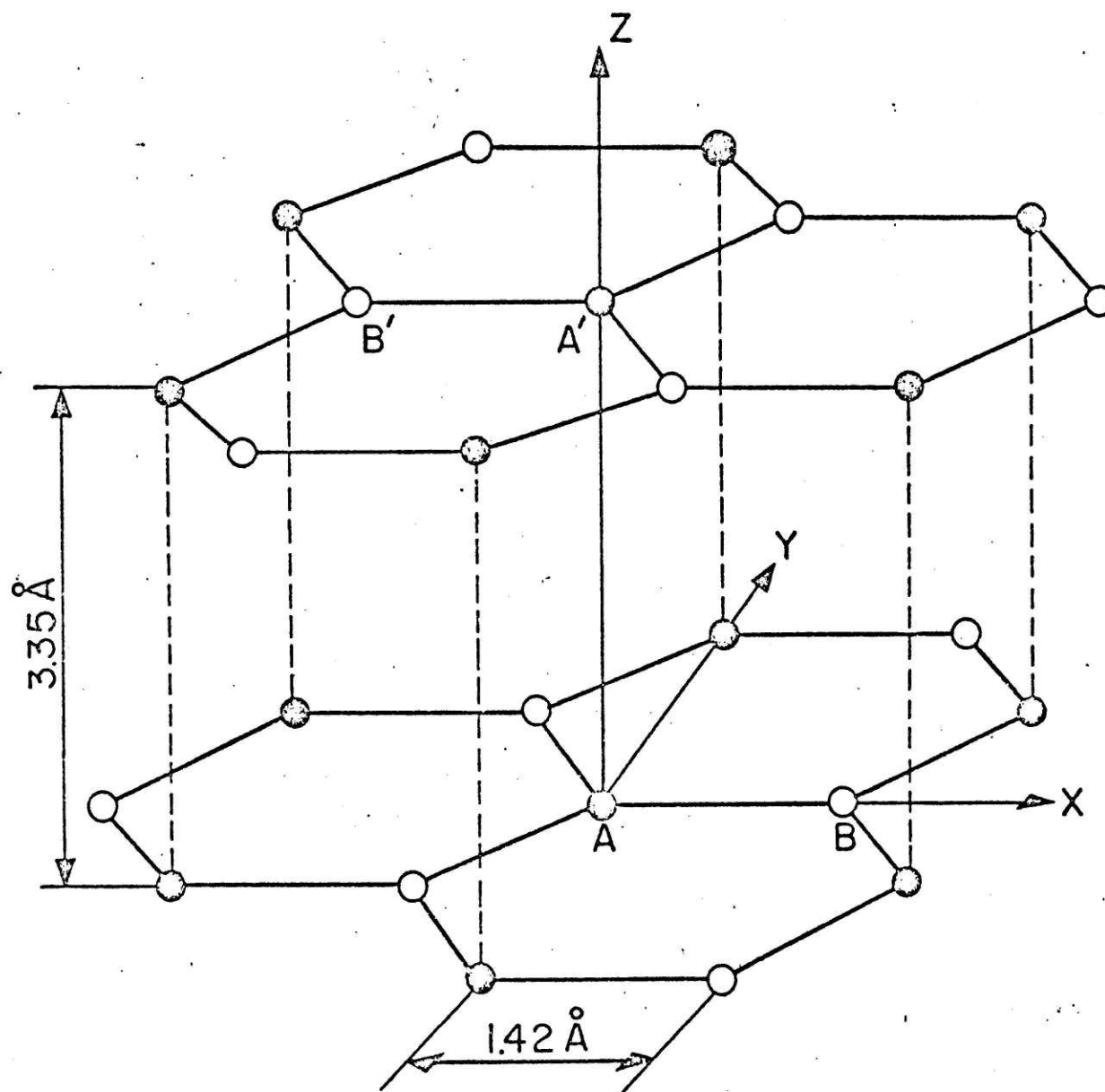
Figure 2.1: Graphite Crystal Lattice
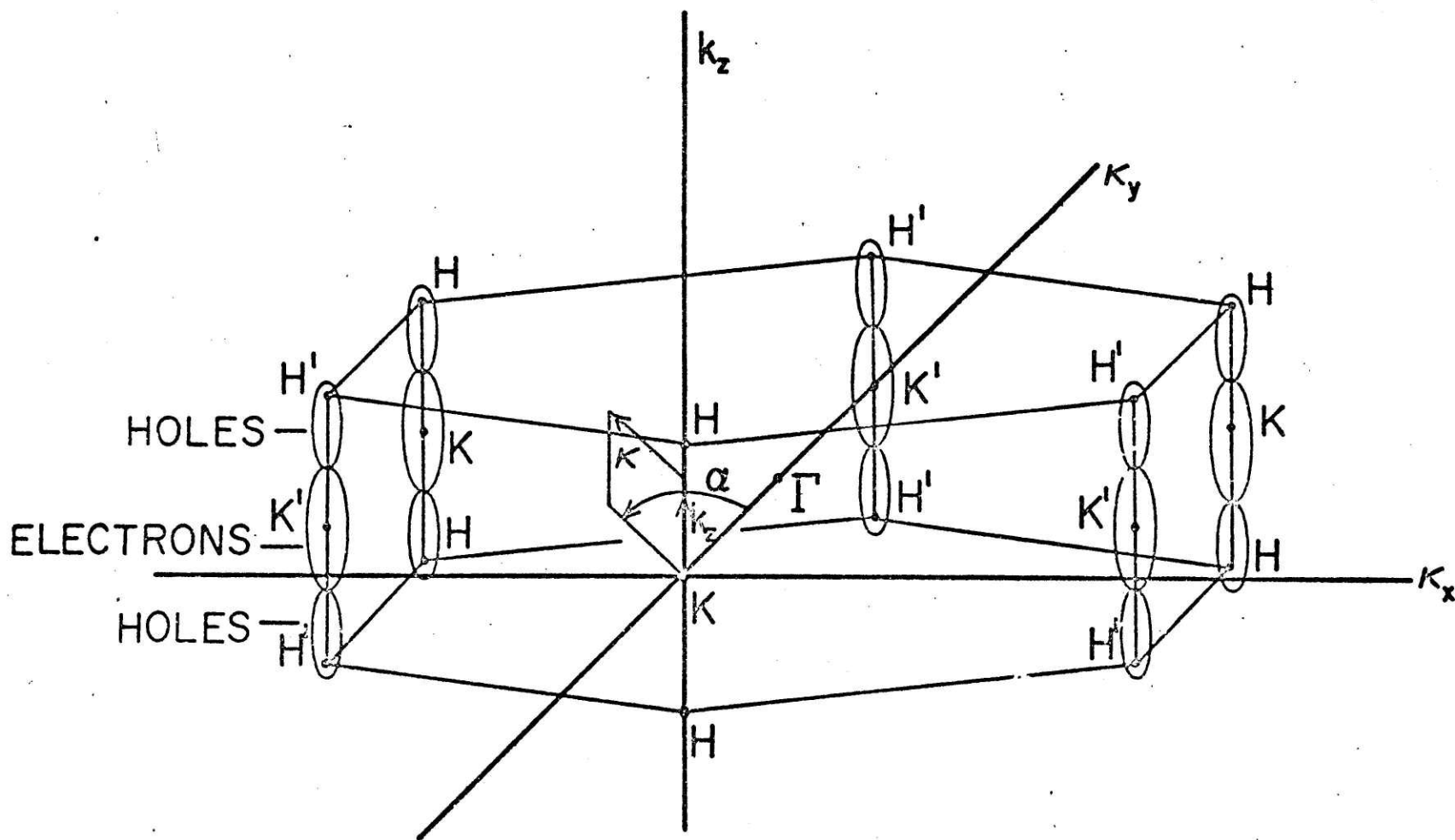
Figure 2.2: Brillouin Zone of Graphite

between layers. The Brillouin zone for a single layer is a two-dimensional hexagon. The 2S, $2P_x$, $2P_y$ atomic wave functions form the bonding and antibonding trigonal orbitals, which make up the σ-bands. The P_z atomic wave functions give rise to two π-bands, which are degenerate at the six Brillouin zone corners. The lower and upper π bands from the valence and the conduction bands, and in the single layer model there is no overlap or band gap between the two bands which are degenerate at the corners of the two-dimensional zone. The energy of interaction between layers is of the order of .5 eV which causes very little change in the overall character of π-bands, whose width is about 20 eV. However, the interaction between layers has a profound effect near the six vertical zone edges where the bandwidth is small and where the carriers are located. There are four π-bands in the three-dimensional band structure of graphite, as there are twice as many atoms in the three-dimensional unit cell. A general model for the behavior of the energy bands near the zone edge was developed by Slonczewski, Weiss and McClure. The Fermi surfaces have very little extent in the x or y direction, so the k·p method was used in xy plane and the tight binding method parallel to the c-axis. Their model can be described by a (4x4) Hamiltonian

$$H = \begin{pmatrix} E_1 & 0 & H_{13} & H_{13}^* \\ 0 & E_2 & H_{23} & -H_{23}^* \\ H_{13}^* & H_{23}^* & E_3 & H_{33} \\ H_{13} & -H_{23} & H_{33}^* & E_3 \end{pmatrix}$$

where

$$E_1 = \Delta + \gamma_1 \Gamma + \frac{1}{2} \gamma_5 \Gamma^2 \qquad (2.1)$$

$$E_2 = \Delta - \gamma_1 \Gamma + \frac{1}{2} \gamma_5 \Gamma^2 \qquad (2.2)$$

$$E_3 = \frac{1}{2} \gamma_2 \Gamma^2 \qquad (2.3)$$

$$H_{13} = \frac{1}{\sqrt{2}} (-\gamma_6 + \gamma_4 \Gamma) \sigma e^{i\alpha} \qquad (2.4)$$

$$H_{23} = \frac{1}{\sqrt{2}} (\gamma_6 + \gamma_4 \Gamma) \sigma e^{i\alpha} \qquad (2.5)$$

$$H_{33} = \gamma_3 \Gamma \sigma e^{i\alpha} \qquad (2.6)$$

$$\Gamma = 2 \cos\left(\frac{1}{2} k_z c\right) \qquad (2.7)$$

The quantity σ is the dimensionless distance from the zone edge, $\sigma = \frac{1}{2}\sqrt{3}\ a\kappa$, where a is the lattice spacing in the plane and κ is the distance in k-space from the zone edge. The quantity α is a polar angle about the zone edge as indicated in figure 2.2. The range of

estimated values of band parameters are:

$$\gamma_0 = 3.16 \text{ eV} \quad ; \qquad \gamma_1 = .39 \text{ eV}$$

$$\gamma_2 = -.019 \text{ eV} \quad ; \qquad \gamma_3 = .14 \text{ to } .29 \text{ eV}$$

$$\gamma_4 = .044 \text{ eV} \quad ; \qquad \gamma_5 = .038 \text{ eV}$$

$$\Delta = -.008 \text{ eV}$$

For the case $\gamma_3 = 0$, the Hamiltonian can be diagonalized easily. The energy in this case is independent of α, so that Fermi surfaces are figures of rotation about the zone edge. Along the zone edge ($\sigma = 0$) the energy is given by the formulas for E_1, E_2 and E_3 (eqs. (2.1), (2.2) and (2.3)). Away from the zone edge, the two highest states increase in energy with increasing σ, while the two lowest states decreases, as shown in figure 2.3. For negative values of γ_2, the lowest energy in the conduction band is at K, and the highest point in the valence band at H. Thus, for pure graphite, there would be electrons around K and holes around H. Introduction of the parameter γ_3 causes the energy to depend upon the polar angle α, the function having trigonal symmetry. Thus the Fermi surface also is trigonally distorted. The Fermi surfaces are quite anisotropic, with the length in the c-direction about 13 times the width perpendicular to the c-axis. Figure 2.4 shows the Fermi surface model for graphite, emphasizing the hole and electron locations and the
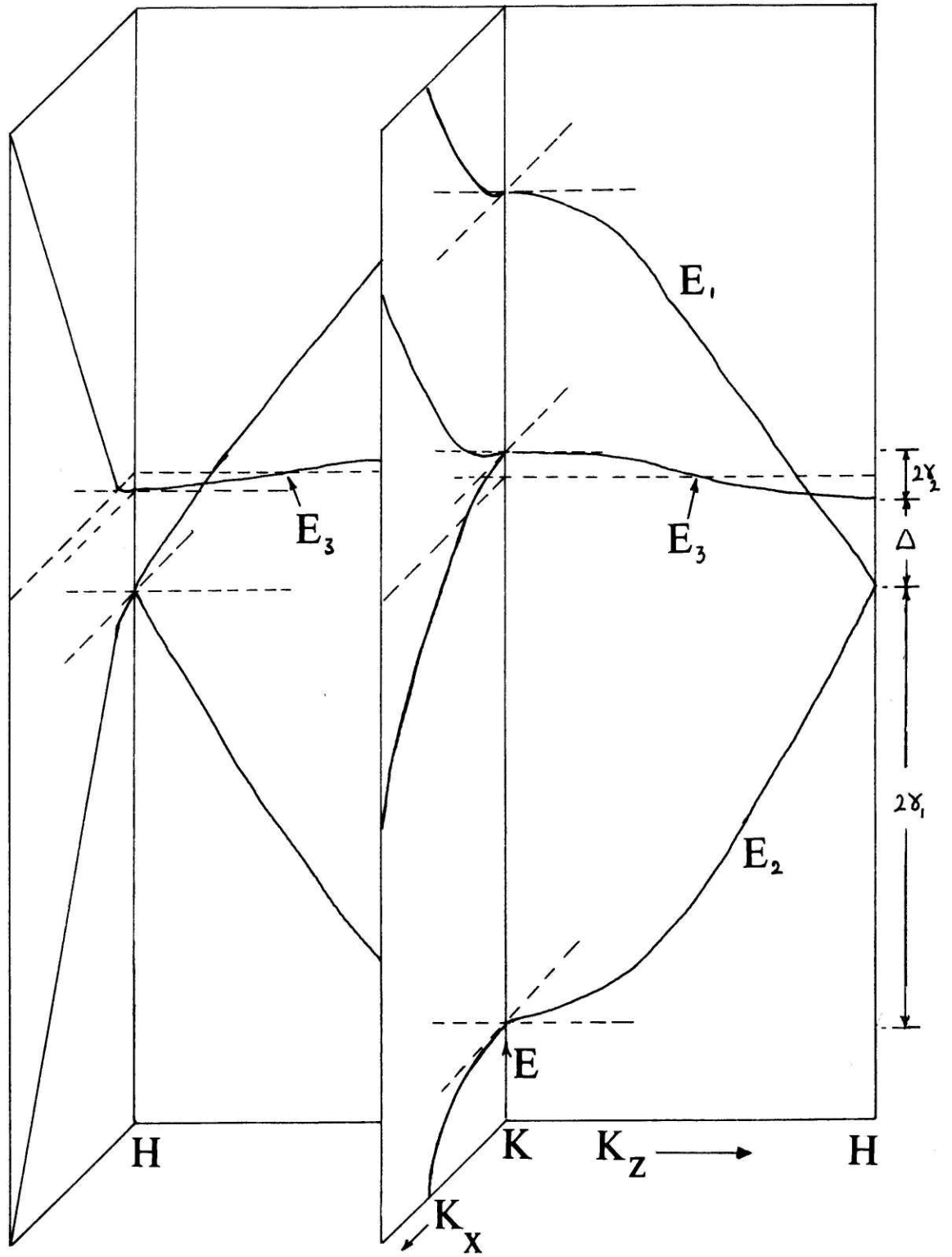
Figure 2.3:   Energy versus Wavenumber for Graphite

k_z

H, ZONE CORNER

$k_z = \dfrac{\pi}{C_o}$

HOLES

EXTREMAL
HOLE
CROSS SECTION

$k_z = 0$
EXTREMAL
ELECTRON
CROSS SECTION

ELECTRONS

$\alpha = 0°$

$\alpha = 120°$
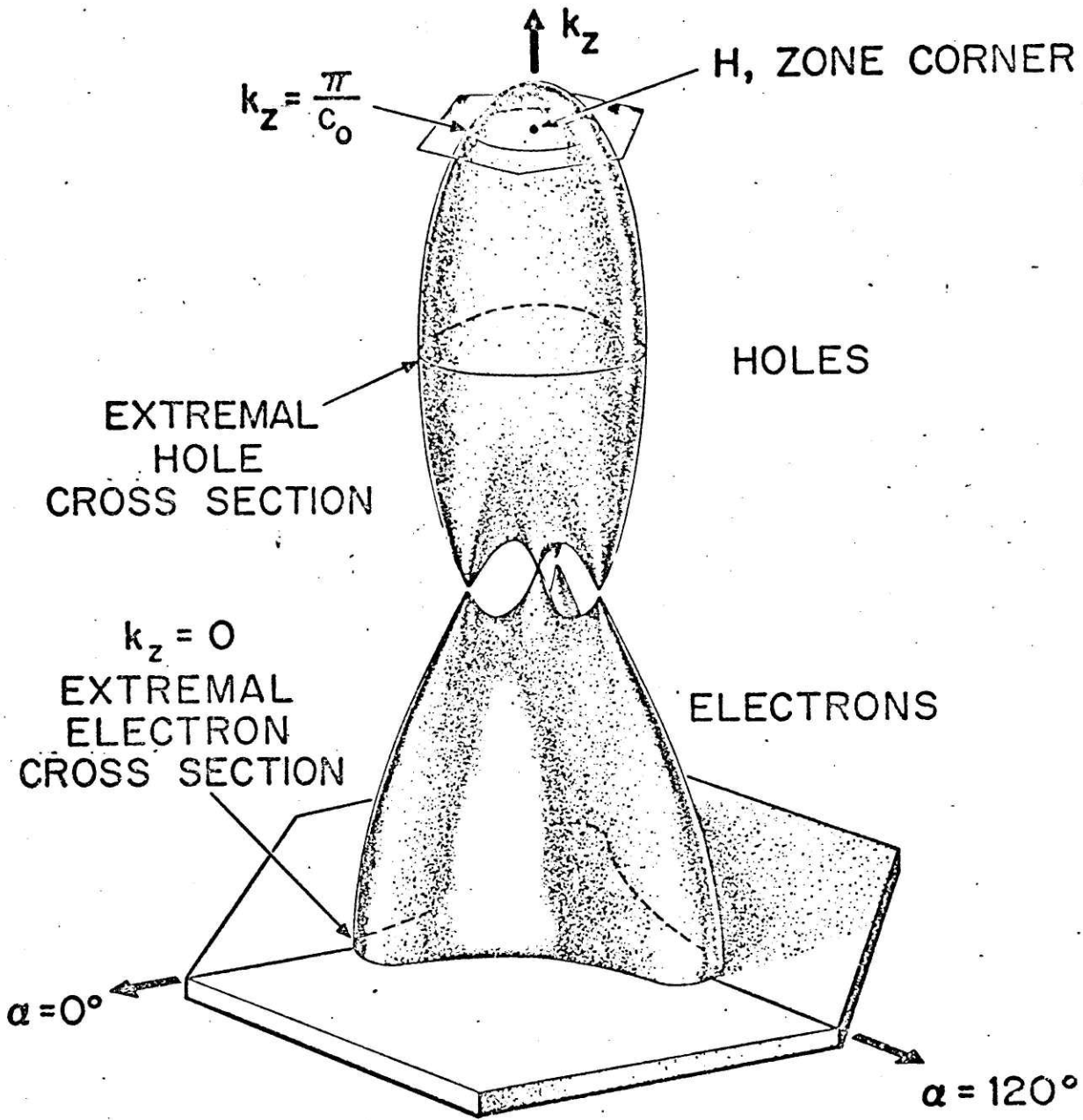
GRAPHITE FERMI SURFACE MODEL

Figure 2.4

trigonal warping.

2.2. Effect of Intercalation in the Dilute Limit

Graphite intercalation compounds consist of an alternating sequence of intercalate monolayers separated by n graphite layer, where n denotes the stage of the compound. We distinguish layers adjacent to the intercalate layers as "bonding layers" whereas the rest of graphite layers are referred to as "interior layers". The question arises to what extent the electronic structure of graphite intercalation compounds can be deduced from a rigid band model modification of the graphite electronic structure. It has been speculated that for low enough intercalate concentrations (called the dilute limit) the electronic structure of the interior layers would resemble that of pure graphite. The electronic interaction between the intercalate monolayers and two adjacent bounding layers is localized within this sandwich. An estimate of the dilute limit follows directly from SWMcC model. The model includes interaction between carbon atoms separated by up to two layer planes. In fact, the band overlap which produces the semimetallic behavior of graphite is associated with the SWMcC band parameter γ_2, representing interaction between atoms two layers apart. Starting at an interior layer and making overlaps corresponding to γ_2 suggests that the SWMcC model, would apply to compounds with stage 5 (3 interior layers and 2 boundary layers) which is an estimate of validity of the dilute limit. A modified SWMcC model can be used to compute the dependence of the SdH extremal
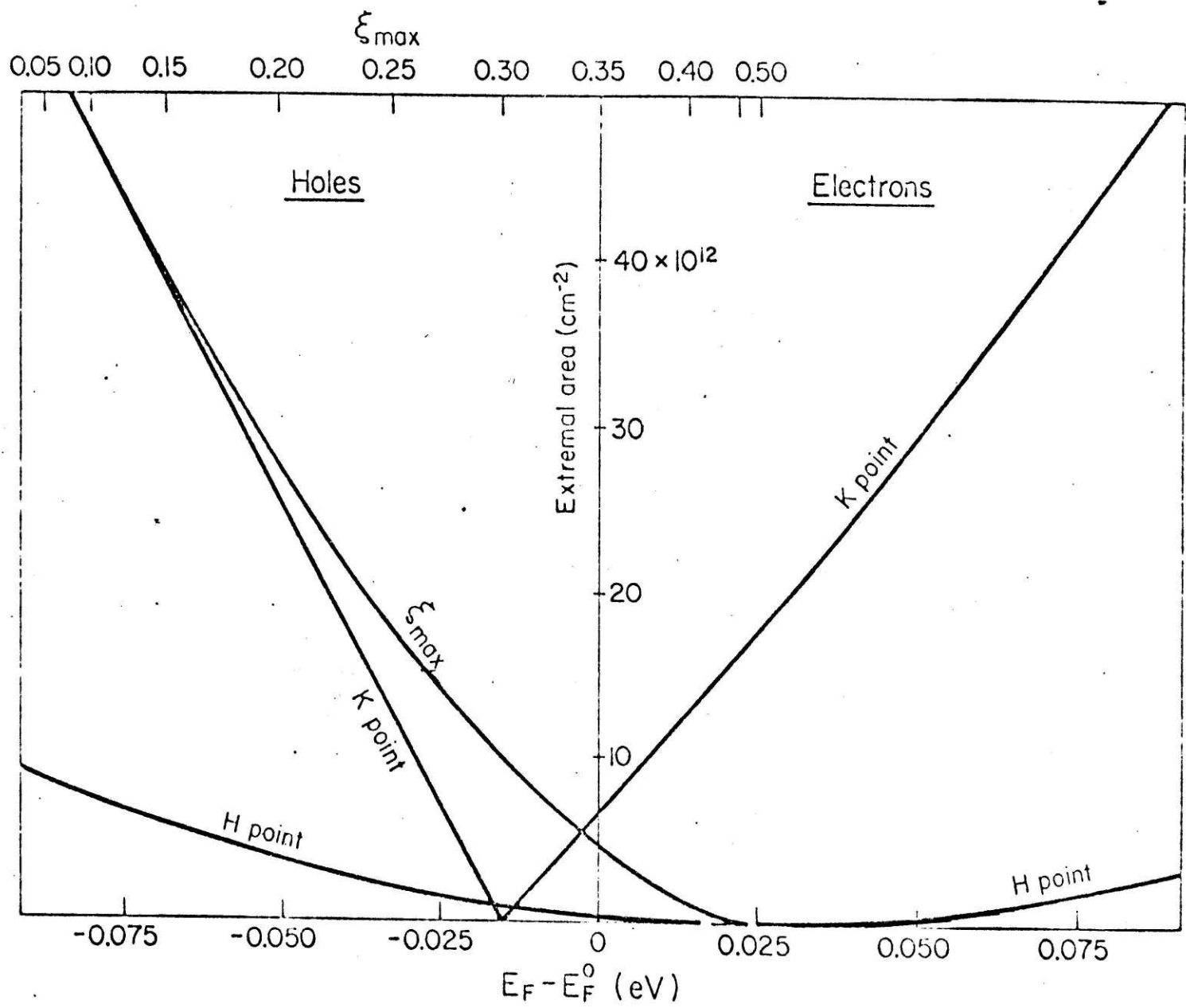
Figure 2.5: External Fermi Surface Cross Sectional area for majority and minority electron and hole pockets versus the change in Fermi energy $E_F - E_F^0$.

areas as a function of Fermi level in the dilute limit (M.S. Dresselhaus, G. Dresselhaus, J.E. Fisher, 1977). Figure 2.5 shows the result of such a calculation. The planes through H and K points and perpendicular to the k-axis always yield extremal cross-sectional areas. There is an additional extremal area associated with the holes (labeled ξ_{max} point) occurring at $\xi = \xi_{max}$, and the values for ξ_{max} corresponding to these extremal areas are given by the upper abscissa scale. As a first approximation, figure 2.5 can be used to estimate the change in the Fermi level as a result of intercalation for the frequencies and the range $f \leq 50$ Tesla.

2.3. A Model for Fermi Surfaces of Graphite Intercalation Compounds

The model described in Section 2.2 is applicable to describe low frequencies (less than 50 Tesla) of dilute compounds ($n \geq 5$). For lower stage compounds and for higher observed frequencies, one has to appeal to band calculations. In the absence of a band calculation for higher stage compounds and with analogy to the pure graphite Fermi surfaces, one can for simplicity make the approximation of an ellipsoidal Fermi surface along the c-axis. The effect of periodic layers of intercalants can be modeled as slices in the ellipsoidal Fermi surface through zone folding effects. Figure 2.6 shows the assumed model for the Fermi surfaces of graphite intercalation compounds. The distance between slices is $\frac{2\pi}{I_c}$ where I_c is the distance between adjacent intercalant layers. Furthermore, at each "cut" strong effect of perturbation "cuts" result in splitting of the surface as is
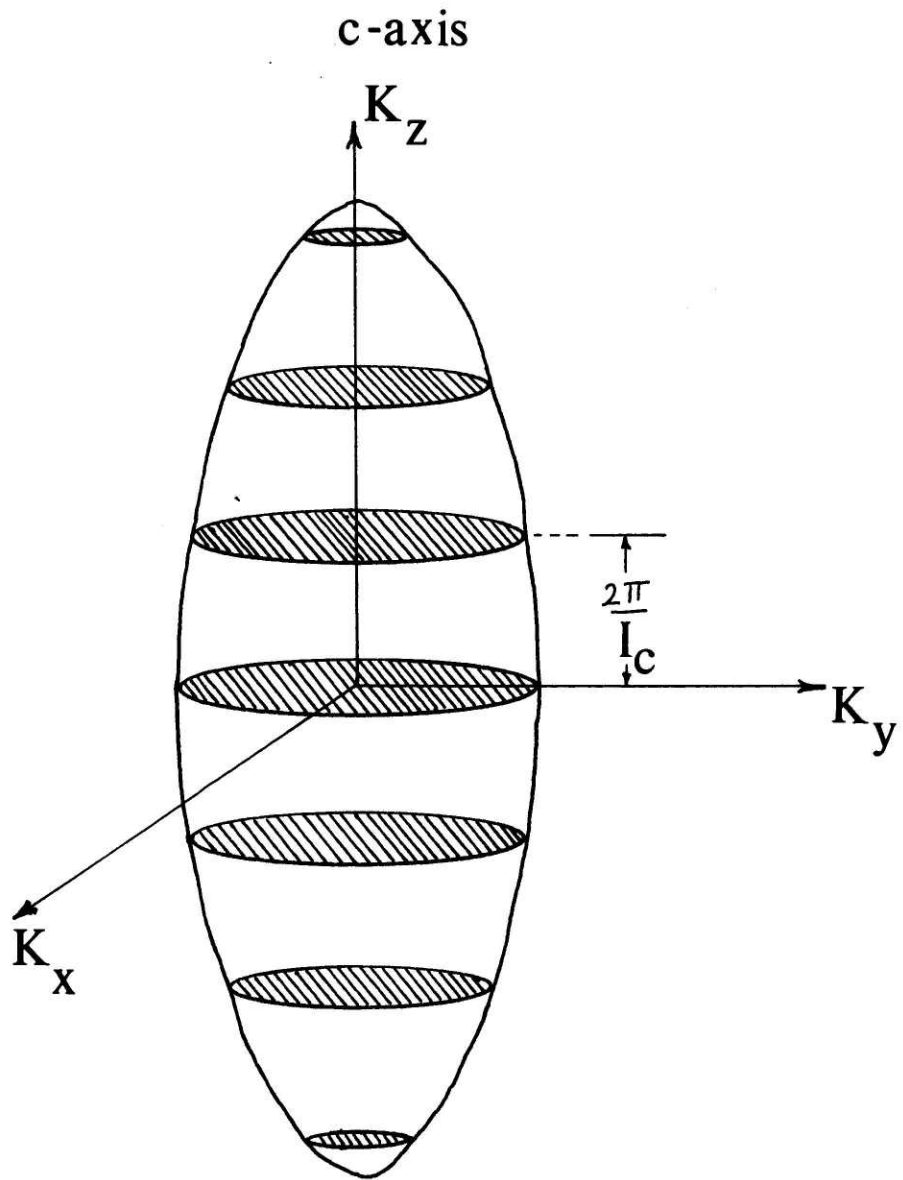
Figure 2.6: A Model for Fermi Surfaces of Graphite Intercalation
Compounds.

Cut

Before Splitting
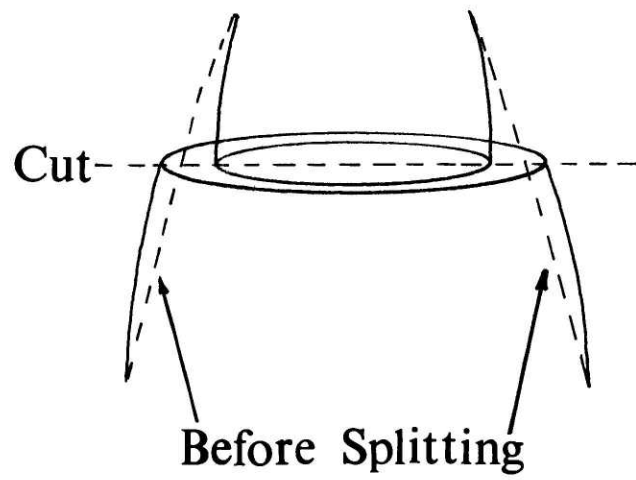
Figure 2.7: Splitting of the Fermi Surface due to the Cut.

illustrated in figure 2.7.

2.4. Shubnikov de-Haas Effect

The Shubnikov de-Haas effect is an oscillatory dependence of the electrical resistivity on the magnetic field. This is produced by the oscillation of the density of states at the Fermi level caused by the quantization of electronic energy levels in the presence of a magnetic field. The oscillations are periodic in inverse field.

If electrons with isotropic effective mass m* a spherical band are exposed to the magnetic field along the z-direction, the energy eigenvalues are

$$E = \left(n + \frac{1}{2}\right)h\omega + \left(\frac{h^2k_z^2}{2m^*}\right) \pm \frac{1}{2} g\mu H \quad ; \qquad n = 0,1,2,\ldots$$

where ω is the cyclotron frequency $\left(\omega = \frac{eH}{m^*c}\right)$, k_z is the wave vector in z-direction ($\vec{H} \quad \hat{z}$-direction), and μ is the Bohr magneton. Due to the quantization of the electron orbit in k-space in a plane perpendicular to the magnetic field the parabolic band is split into subbands which are separated in energy by the amount $h\omega_c$. The uniform distribution of quantum states in k-space in the field-free case is replaced by a series of interlocking Landau cylinders with the cross section A_n in the direction perpendicular to the magnetic field:

$$A_n = (n + \gamma)\left(\frac{2\pi eH}{hc}\right)$$

γ is $\frac{1}{2}$ for perfectly free electrons since the Schrodinger equation
for the orbital motion in the magnetic field reduces to that of the
harmonic oscillator problem, for which the energy eigenvalues are
$(n + \frac{1}{2})h\omega_c$. γ is also $\frac{1}{2}$ for electrons which obey a general quadratic
dispersion law. This is often the case for states near band extrema.
γ is very close to $\frac{1}{2}$ even for a Fermi surface of arbitrary shape
(A.V. Gold). The discrete nature of the Landau cylinder is smeared
out unless the Landau level separation $h\omega_c$ is larger than k_BT. Another
requirement for the observation of the quantum effect is that complete
orbits in k-space be performed by the electrons before they are scattered,
which can be formulated by the condition $\omega\tau \gg 1$, where τ is the
relaxation time. The condensation of quantum states into the Landau
cylinders in the magnetic field has drastic consequences on the density
of states. Ignoring the spin, the density of states per unit energy
and unit volume is of the form:

$$g(E) = \frac{1}{2}\left(\frac{1}{2\pi}\right)^2\left(\frac{2m^*}{h^2}\right)^{3/2} \sum_{n=0}^{n_{max}} \frac{h\omega}{\left[E - \left(n + \frac{1}{2}\right)h\omega\right]^{1/2}}$$

The summation is done over all occupied magnetic subbands.
Whenever the energy coincides with that of a Landau level extremum
the density of states diverges. The divergence is due to an
oversimplification which neglects the finite width of the Landau levels
due to collision broadening. The oscillation in the density of states
as a function of the magnetic field can strongly affect the scattering

rate of electrons and produce oscillation in the transport properties. A maximum in the scattering (and consequently, maximum in resistance) occurs in a longitudinal magnetic field whenever the Fermi level coincides with the Landau subband extremum. Provided that the Fermi level remains constant independent of H, the oscillations in the resistivity are periodic in inverse field. The oscillations in the transverse magnetoresistance are also periodic in inverse field. The period in both cases is for the simplest model of a solid

$$\Delta\left(\frac{1}{H}\right) = \frac{he}{m^*c}\frac{1}{E_F} = \frac{2\pi e}{hc}\frac{1}{\left(\frac{2\pi}{h^2}m^*E_F\right)} = \frac{2\pi e}{hc}\frac{1}{A}$$

where A is the extremal cross section of the spherical Fermi surface. This result has been generalized for Fermi surfaces of rather general shape (Onsager, 1952). For a general Fermi surface, the quantum oscillations in different parts of the Fermi surfaces will interfere destructively except at the extremal cross section. Therefore, the more general relation holds

$$\Delta\left(\frac{1}{H}\right) = \frac{2\pi e}{hc}\frac{1}{A_{extr.}}$$

where A_{extr} is the extremal area of the Fermi surface perpendicular to the magnetic field. The Fermi level remains constant as long as $\frac{E_F}{h\omega_c} \gg 1$.

The most general form of the resistivity in a magnetic field

is due to Lifschitz and Kosevich (1956) and has the following form for the ith carrier

$$\rho_i = H^{\ell_i} \sum_{r=1}^{\infty} B_i(r) \frac{rU_i}{\sinh rU_i} \exp\left(- \frac{rU_i}{T} T_D\right) \cos\left(\frac{rch}{e} \frac{A_i}{H} - \phi_i(r)\right)$$

where $B_i(r)$ is the amplitude of the rth harmonic of the ith carrier, $\omega_i = \frac{eH}{m_i^* c}$ is the cyclotron frequency at the Fermi surface extremum for the ith carrier, $U_i = \frac{2\pi^2 k_B T}{\hbar\omega_i}$, $k_B T_D$ is the collision broadening of the Landau levels which is characterized by the Dingle temperature T_D, A_i the extremal cross section of the Fermi surface, and $\phi_i(r)$ is a phase factor. The appearance of $\frac{rU_i}{\sinh rU_i}$ is due to the fact that we are not at zero temperature, and ℓ_i is determined by a particular mechanism for electron scattering. The total resistivity is then the sum of the damped oscillatory terms ρ_i which are periodic in inverse magnetic field and a background non-oscillatory term ρ_B, namely

$$\rho_{Total} = \sum_i \rho_i + \rho_B \quad .$$

Thus, in order to obtain extremal cross sectional areas of Fermi surfaces, one has to obtain the power spectrum of the oscillatory part of the resistivity.

CHAPTER 3

DESCRIPTION OF THE EXPERIMENT

In this chapter, we will describe the experimental details for the measurement of electrical resistivity (ρ) and of the derivative of electrical resistivity with respect to magnetic field $\left(\frac{\partial\rho}{\partial H}\right)$ as a function of magnetic field where the focus is on the oscillatory behavior with field (Shubnikov de-Haas effect) rather than the background values of (ρ) and $\left(\frac{\partial\rho}{\partial H}\right)$.

In the first section of this chapter, we will describe the experimental details of electrical resistivity measurements. The second section illustrates the modulation technique while the third section deals with data analysis.

3.1. Electrical Resistivity as a Function of Magnetic Field

Resistivity measurements were made for the magnetic field range $0 < H < 14$ T while the samples were immersed in liquid Helium (4.2K). Four contacts A, B, C and D were connected as shown in figure 3.1. A constant current flows from A to D within the a-planes of the sample and the voltage is measured across B and C. V_{BC} is, then, proportional to the electrical resistivity of the sample. The magnetoresistance is measured as a function of the magnetic field. Measurements were made with H at various angles θ with respect to the c-axis of the sample.
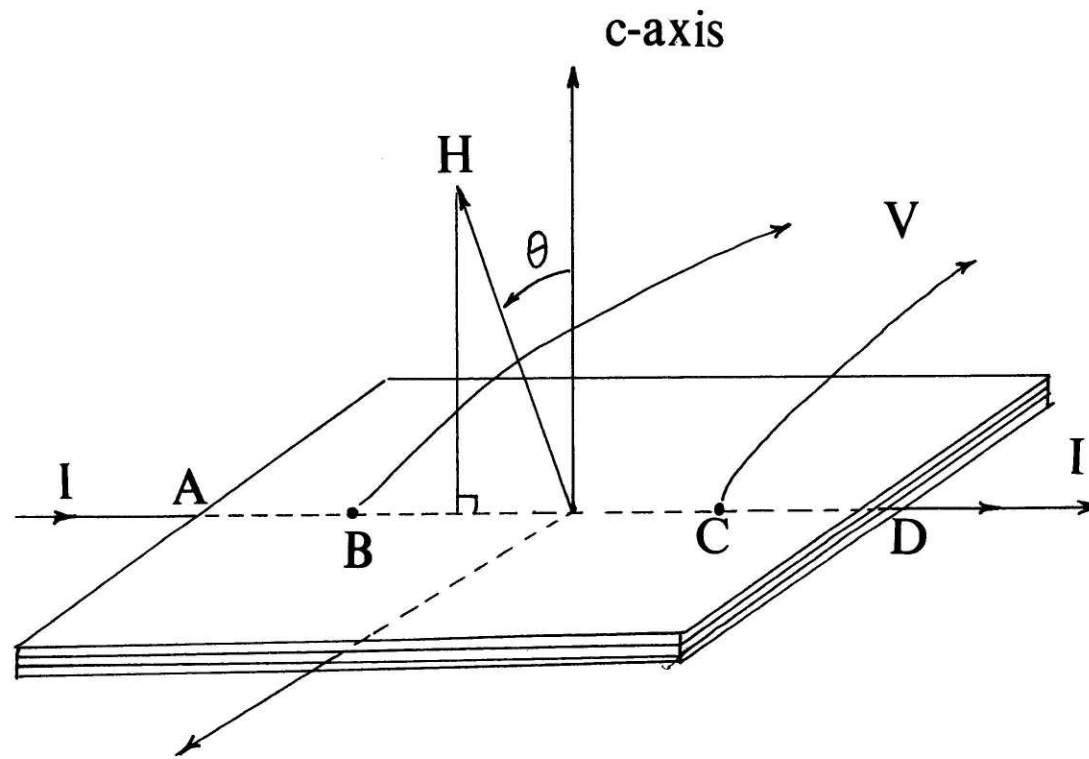
Figure 3.1: Geometry of Sample with Respect to the Magnetic Field.

Figure 3.2 shows the DC magnetoresistance setup. The setup consists of a current source (1 mA - 2 A), DC amplifier, x-y recorder, A/D convertor, and a cartridge tape drive. For the measurements, we used a KEPCO Current Regulator cc-7-2M as a current source, a Keithley 140 (precision nanovolts) as the DC amplifier, a Philips PM8125 x-y recorder, and Columbia 300B was used as a tape drive (recorder). The outputs of A/D convertors were recorded on the magnetic tape of the tape drive. The magnetic field was measured by an output voltage proportional to the current flowing in the magnet. The voltage proportional to magnetic field was taken directly from the control console. The relationship between the current in the magnet and magnetic field is provided for the cell magnets used.

Ohmic contacts were bonded onto the sample using conductive paint (Dupont #4929). The sample was mounted on a sample holder attached to a dip stick, and immersed in liquid helium contained in a storage Dewar. The current source was set typically at 50 mA. The output voltage from the DC-amplifier which provided the resistivity and the output voltage proportional to the magnetic field was sampled typically at the rate of eight pairs per second and was recorded on magnetic tape. The magnetic field was typically swept at the rate of 1.4 Tesla per minute.

To the magnet ← CONSOLE → Voltage proportional to magnetic field

V_{BC}

DC AMPLIFIER

x-y RECORDER

liquid He

MAGNET

V

SAMPLE

CURRENT SOURCE

A/D CONVERTOR

COLUMBIA 300 TAPE DRIVE

Figure 3.2: DC Magnetoresistance Setup

3.2. Derivative of Resistivity as a Function of Magnetic Field

The amplitude of the SdH oscillations decreases with increasing sample rotation angle θ of H with respect to the magnetic field. In order to observe the oscillations at higher angles, we had to appeal to the modulation technique which yields the derivative of resistivity with respect to magnetic field rather than the resistivity itself.

Modulation Technique

In this method, the sample geometry remains the same as in the previous method. However, a small 7.5 Hz sinusoidal magnetic field is superimposed on the sweeping magnetic field. The output voltage V_{BC} is detected (Fig. 3.1) by a lock-in amplifier tuned at a frequency of 7.5 Hz. V_{BC} is, then, proportional to the derivative of the electrical resistivity with respect to magnetic field.
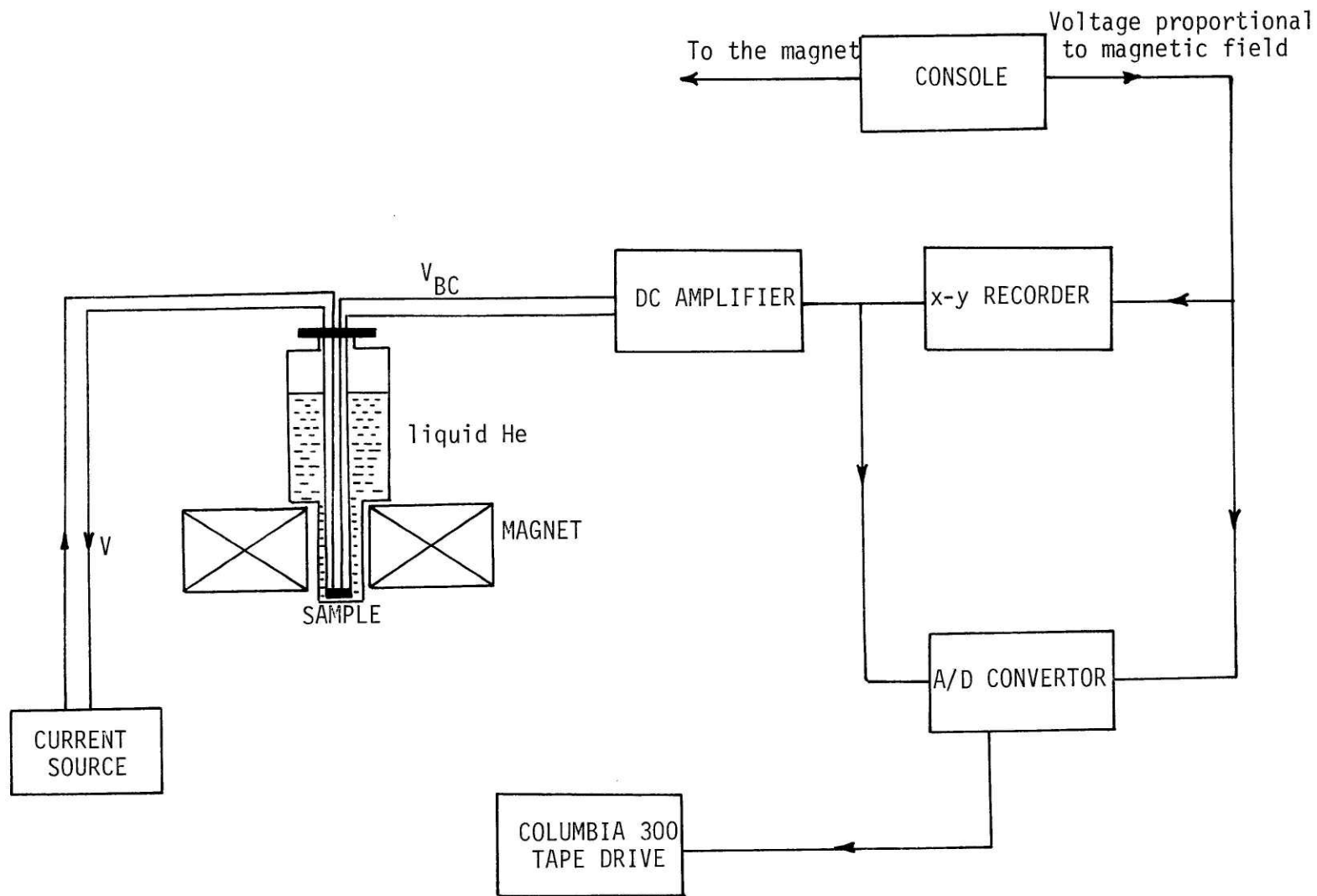
Figure 3.3 shows the experimental setup. The setup contains the same new elements. An ITHACO Dynatrac 391A lock-in amplifier were used for detection of 7.5 Hz frequency component of V_{BC} (Fig. 3.1) which is proportional to the derivative of resistivity $\left(\frac{\partial \rho}{\partial H}\right)$. A frequency divider and General Radio 1310-B oscillator are used to produce a stable 7.5 Hz modulating signal to drive the reference of the lock-in amplifier as well as the oscillatory part of the sweeping magnetic field. The frequency divider divides the 60 Hz line frequency by 8 (7.5 Hz) and by coupling to the oscillator makes it possible to have a stable 7.5 Hz oscillator output provided that the oscilator frequency is set in the interval 7 Hz < f < 8 Hz. A general radio decade voltage divider 1454-AH was used to reduce the
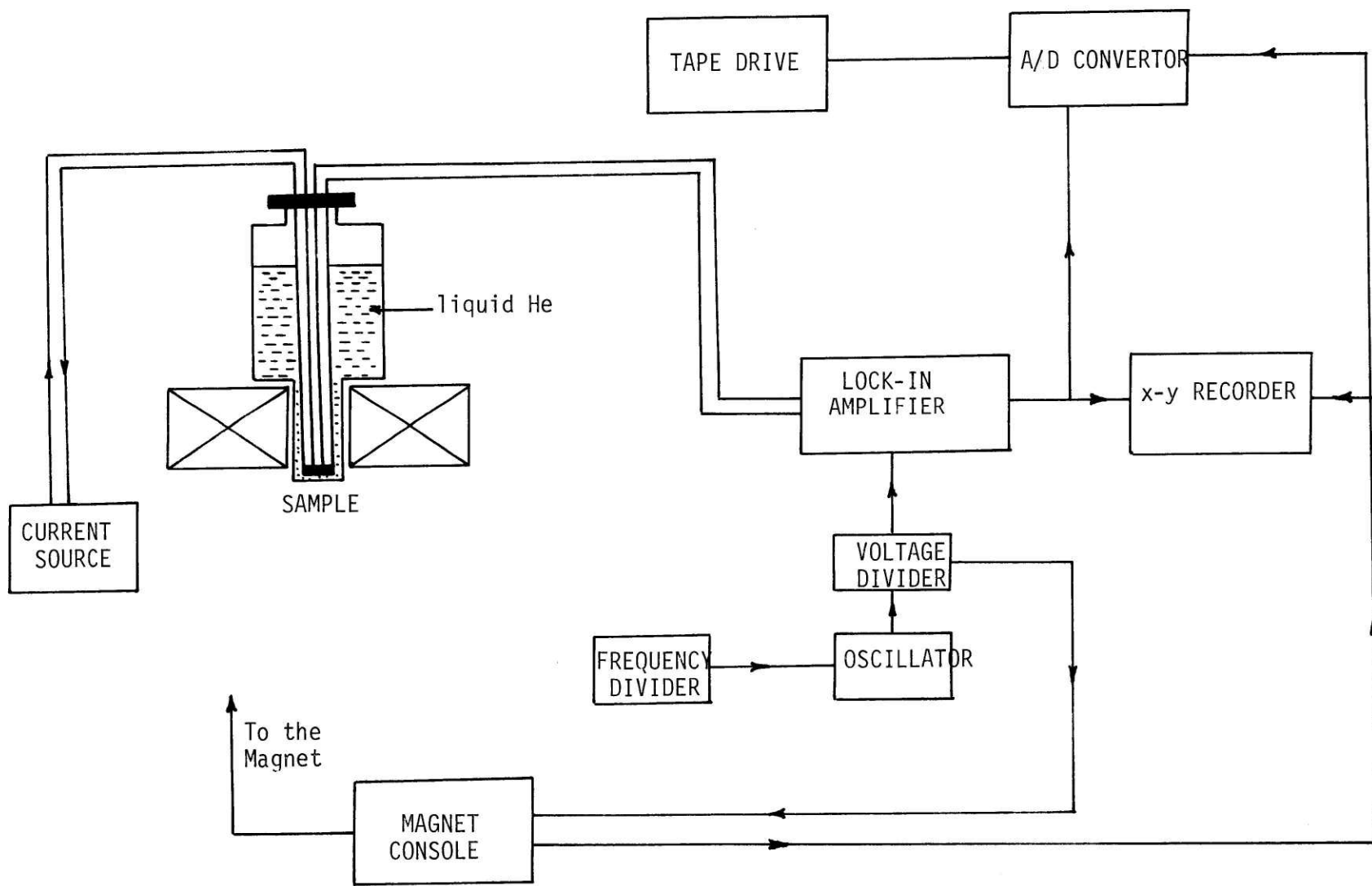
Figure 3.3: AC Magnetoresistance Setup

voltage to the console which drives the oscillatory part of the
magnetic field. Care was taken to choose the amplitude of the oscillatory
part of the magnetic field as small as possible in order not to lose
the fine structure of $\frac{\partial \rho}{\partial H}$ and at the same time large enough to produce a
reasonable signal. One source of noise can be the currents induced in
the wires attached to the four contacts by the oscillatory component
of the magnetic field. This noise can be reduced if two woven wires
with opposite helicity are used instead of a single wire. The output
of the lock-in amplifier (proportional to $\frac{\partial \rho}{\partial H}$) and the output of voltage
out of the console which is proportional to the magnetic field (described
in the previous section) were sampled at the rate of typically eight
pairs per second and recorded on the magnetic tape (via the Colombia
300 tape drive) to yield the magnetic dependence of $\frac{\partial \rho}{\partial H}$.

3.3. Data Reduction

In this section, we will discuss the data reduction system. The
analysis is done on a PDP/11 computer at the National Magnet Labortory.
The data analysis yields the frequencies and relative amplitudes of
SdH oscillations. The data reduction procedure consists of the removal
of the non-oscillatory part of the signal (magnetoresistance or its
derivative), inversion of the magnetic field, and subsequent Fourier
transformation.

Details of the Data Analysis

The data on the magnetic tape contains the signal and voltage
proportional to the magnetic field as pairs. The pairs are read into

the computer and stored on floppy disks (NASCHUA 2200-20) with the help

of a tape drive (Colombia 300B) linked to the PDP/11. The program to

activate the tape drive is COPY.LDA[200,20] which was written by Don

Nelson. The data analysis is done using the Rubin System One (RS1)

program (also written by Don Nelson). This program carries a host of

other subprograms essential in data reduction. This program can

accommodate a maximum of 1024 pairs of integers. There are typically

5000 pairs for a ten minute magnet sweep. The number of data pairs is

reduced to a number that can be handled by RS1 through an averaging

procedure carried out by calling the SFAVE[200,20] program. This program

averages the signal values in equal intervals of magnetic field. With

an appropriately chosen interval, the data can be reduced to be

accommodated by RS1. This step reduces the maximum frequency cutoff

from 2.5×10^5 Tesla to 5×10^4 Tesla which is much larger than the largest

frequency observed (~10 Tesla). Thus, in averaging the data no essential

features are lost. Having inputted the reduced data into RS1 the

non-oscillatory part of the signal can be eliminated by first fitting

a second order polynomial to the pairs and subsequent subtraction of

this polynomial. The voltage values proportional to the magnetic field

range from zero to 20,000. Since RS1 rounds off floating point numbers,

an arbitrary constant $2^{14} = 16,384$, rather than unity, is divided by

the magnetic field values to avoid loss of the significant figures.

Upon this division, RS1 gives another scaling value automatically, which

must be kept track of. The data processed so far which is the oscillatory

part of the signal versus the scaled inverse field is not distributed

in equal intervals (non-uniform data). The above non-uniform data is made into uniform (equidistance) data of length 1024 through an interpolation scheme in RS1. Having subtracted the DC part of the uniform data, the data is then Fourier analyzed to yield the Fourier power spectrum of the SdH oscillations. Since the processed data before the Fourier transformation was scaled, the power spectrum should be appropriately scaled to yield the true power spectrum. The resolution of the power spectrum is

$$\Delta F = \frac{1}{\frac{1}{H_\ell} - \frac{1}{H_h}}$$

where H_ℓ and H_h are lower and upper bounds of magnetic field in the experiment. The resolution of the spectrum is mainly determined by the lower bound of the magnetic field where there are still observable oscillations. For a typical case, H_h = 14 T and H_ℓ = 2 T (fig. 3.4).
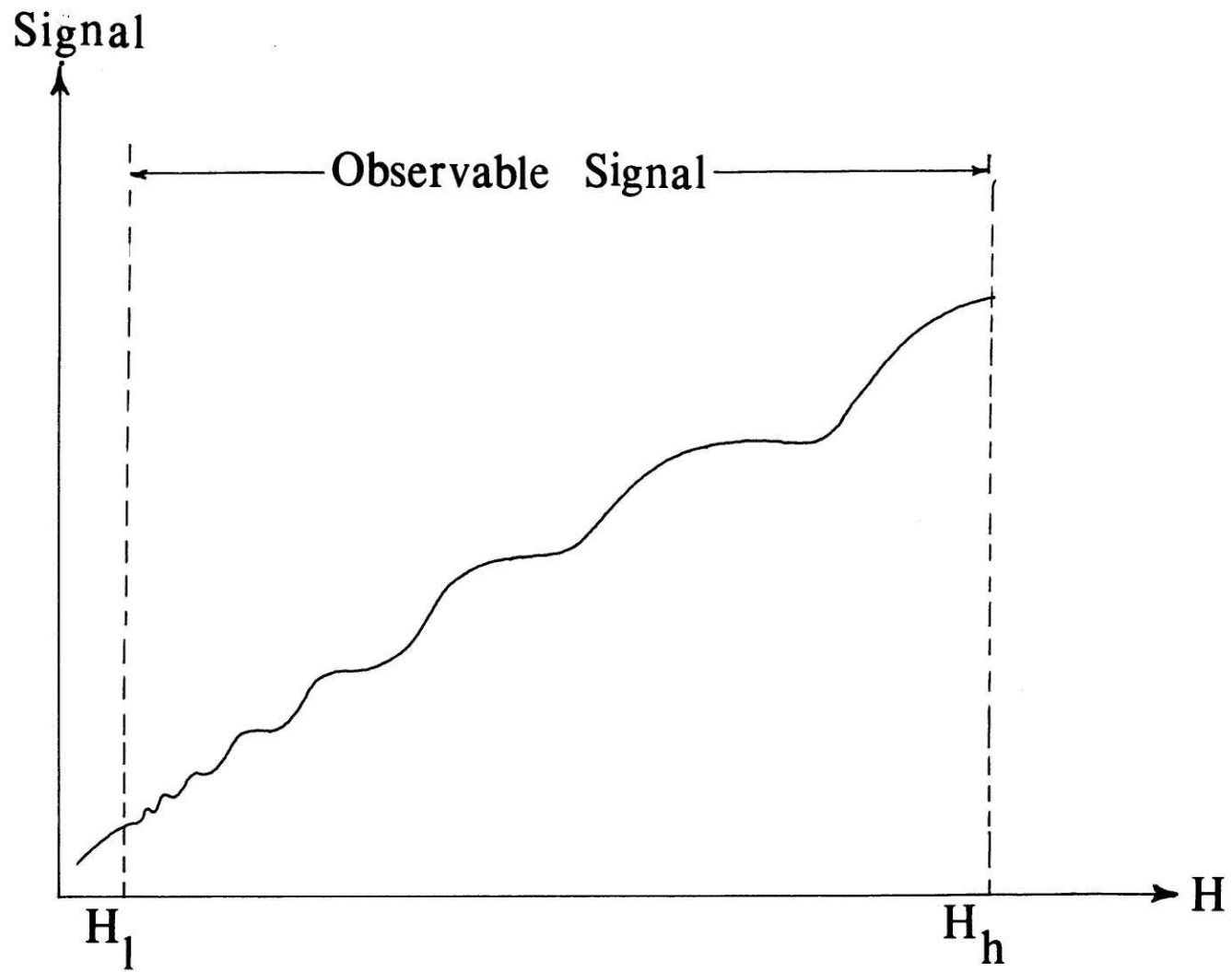
Figure 3.4: The Region of Observed Shubnikov de Haas Oscillations.

Therefore the best resolution one can obtain for a typical signal is $\Delta F \approx 1$ Tesla. However, this maximum resolution can be achieved through a program that can accommodate more points than 1024 points (RS1 progam).

CHAPTER 4

EXPERIMENTAL RESULTS

In this chapter, we shall report the results of stage, angular, and intercalant dependence of the Shubnikov-de Haas effect in graphite intercalation compounds. The materials to be studied are C_xFeCl_3, C_xPdCl_2, C_xBr_2, C_xRb, and C_xAlCl_3. The details of the results for the above compounds shall be illustrated in section 4.1. We shall explore a possible model of G.I.C. in section 4.2.

4.1. SdH Results

The results of the SdH measurements made on the above materials are shown in figures 4.1 to 4.9. Figure 4.1 shows some typical SdH oscillations (C_xPdCl_2 Stage-3) as a function of angle and figure 4.2 illustrates the corresponding power spectra. As one notes in figure 4.2 that as θ is increased the structural features labelled 1 and 2 are displaced toward higher frequencies. The results of the angular dependence of several of the SdH frequencies for C_xFed_3 (Stage 1, 3, and 7), C_xPdCl_2, C_xBr_2, C_xAlCl_3, and C_xRb are shown in figures 4.3, 4.4, 4.5, 4.6, 4.7, 4.8, and 4.9, respectively.

The results of the SdH measurements on C_xFeCl_3 (Stage 1, 3, and 7) are summarized in tables 4.1 to 4.3. The tables contain only the frequencies with large amplitudes in the power spectra of SdH

Angular Dependence of C_xPdCl_2 Stage 3

$\theta = 0°$

$\theta = 20°$

$\theta = 30°$

Intensity (Arb. units)

Magnetic Field (Tesla)
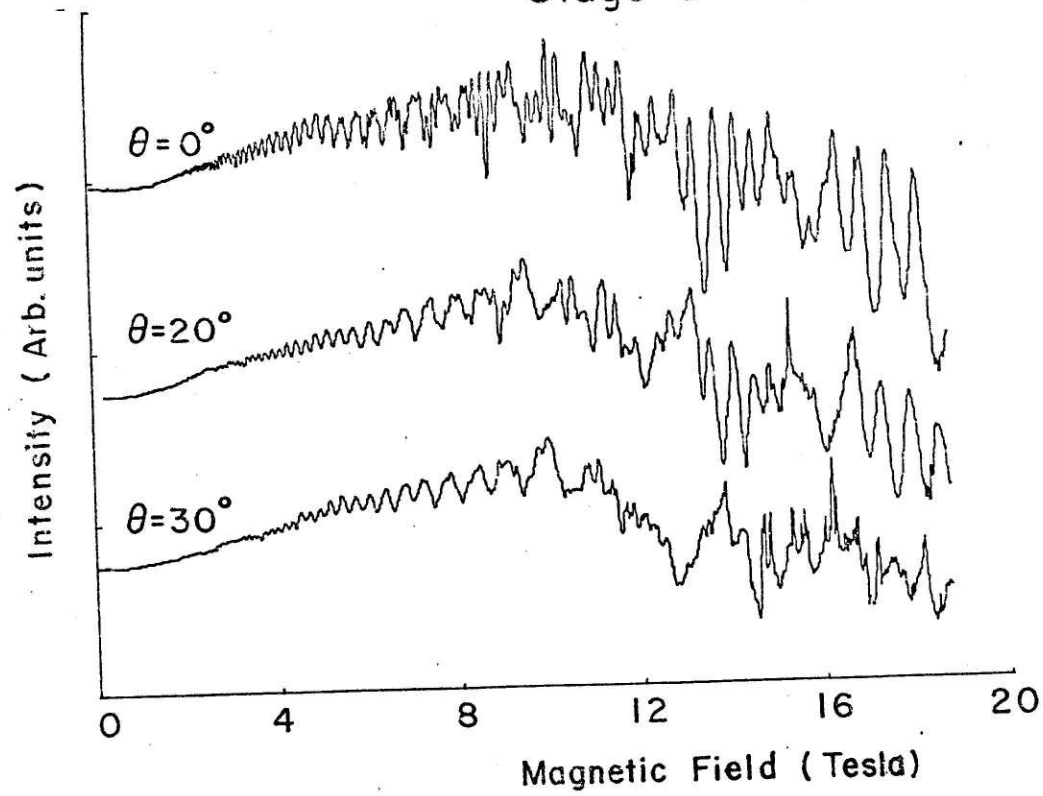
Figure 4.1: Typical Shubnikov de Haas Oscillations (C_xPdCl_2 - Stage 3, $\theta = 0°$, $20°$ and $30°$).

Angular Dependence of Stage 3 C_xPdCl_2
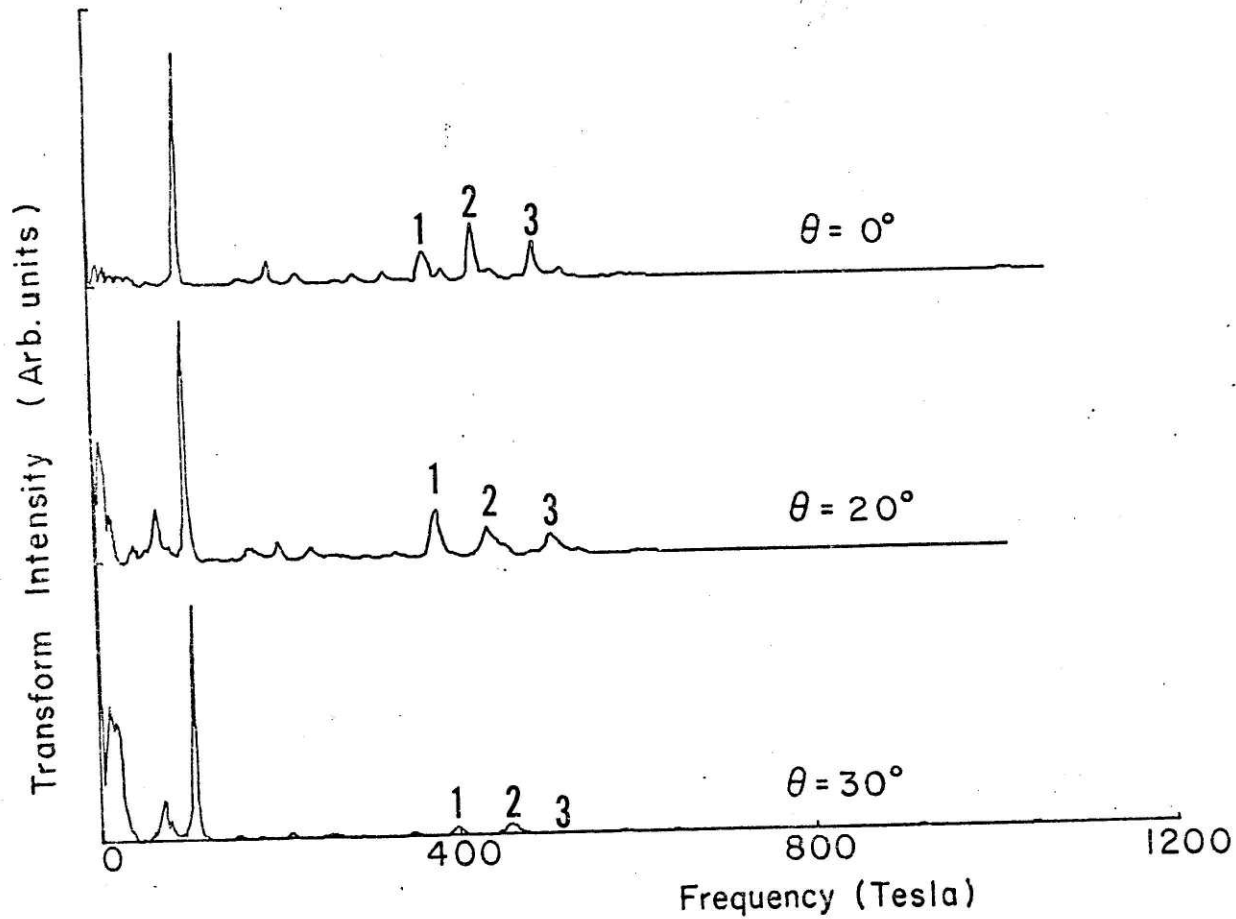
Figure 4.2: Typical Power Spectrum of the Shubnikov de Haas Oscillations

(C_xPdCl_2 - Stage 3, θ = 0°, 20°, and 30°).
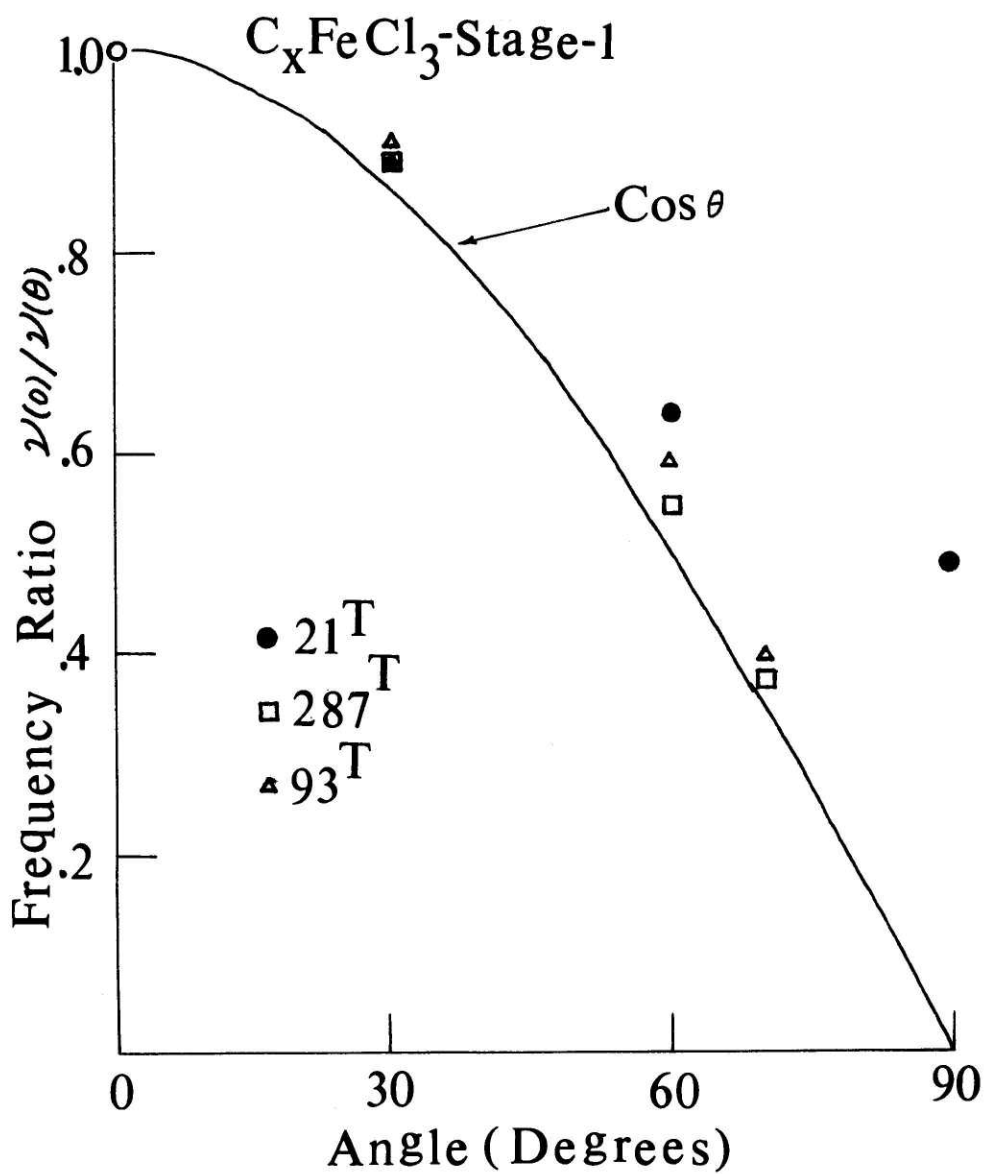
Figure 4.3: $\nu(0)/\nu(\theta)$ vs. Angle for C_xFeCl_3 - Stage 1.
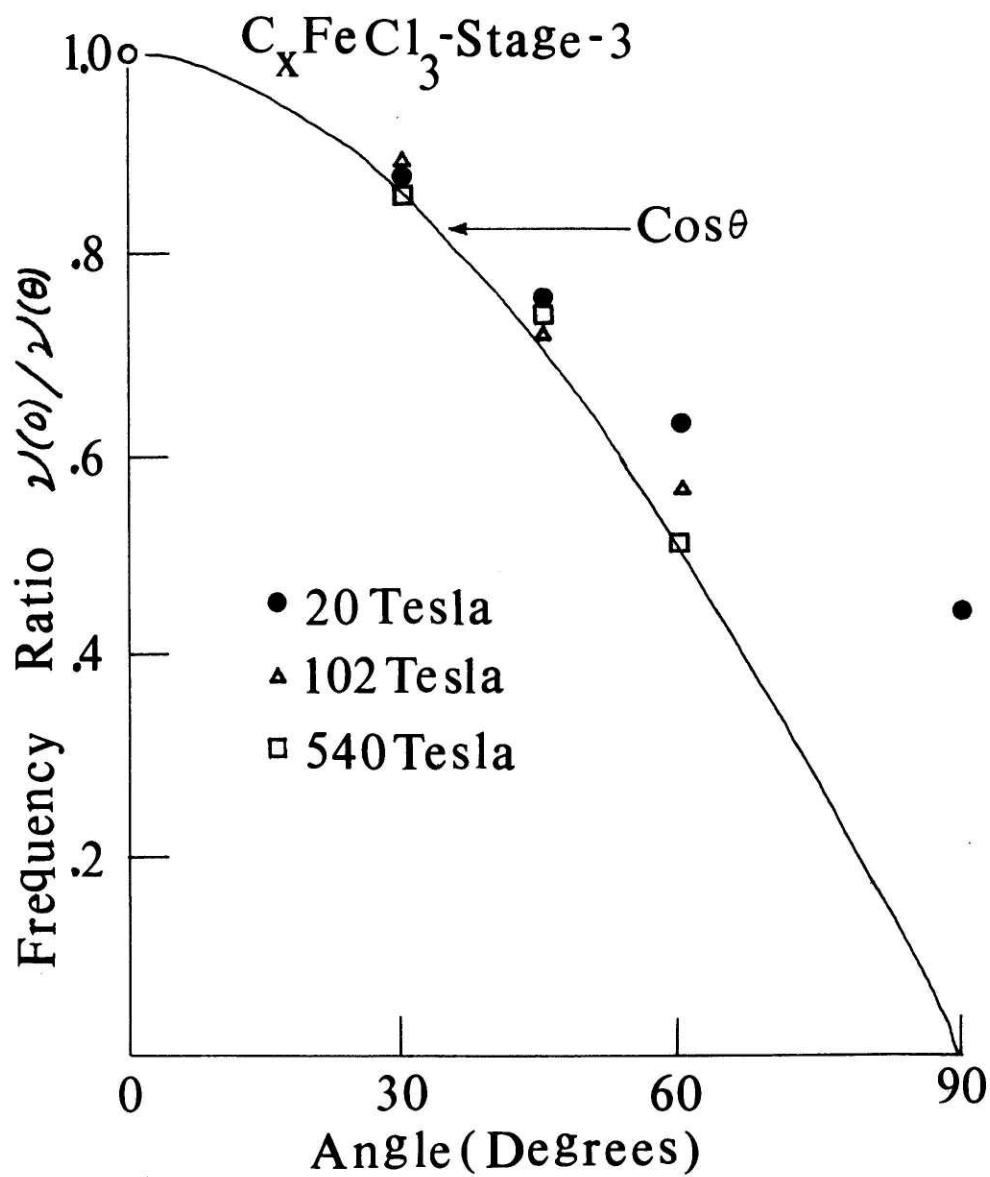
Figure 4.4: $\nu(0)/\nu(\theta)$ vs. Angle for C_xFeCl_3 - Stage 3.
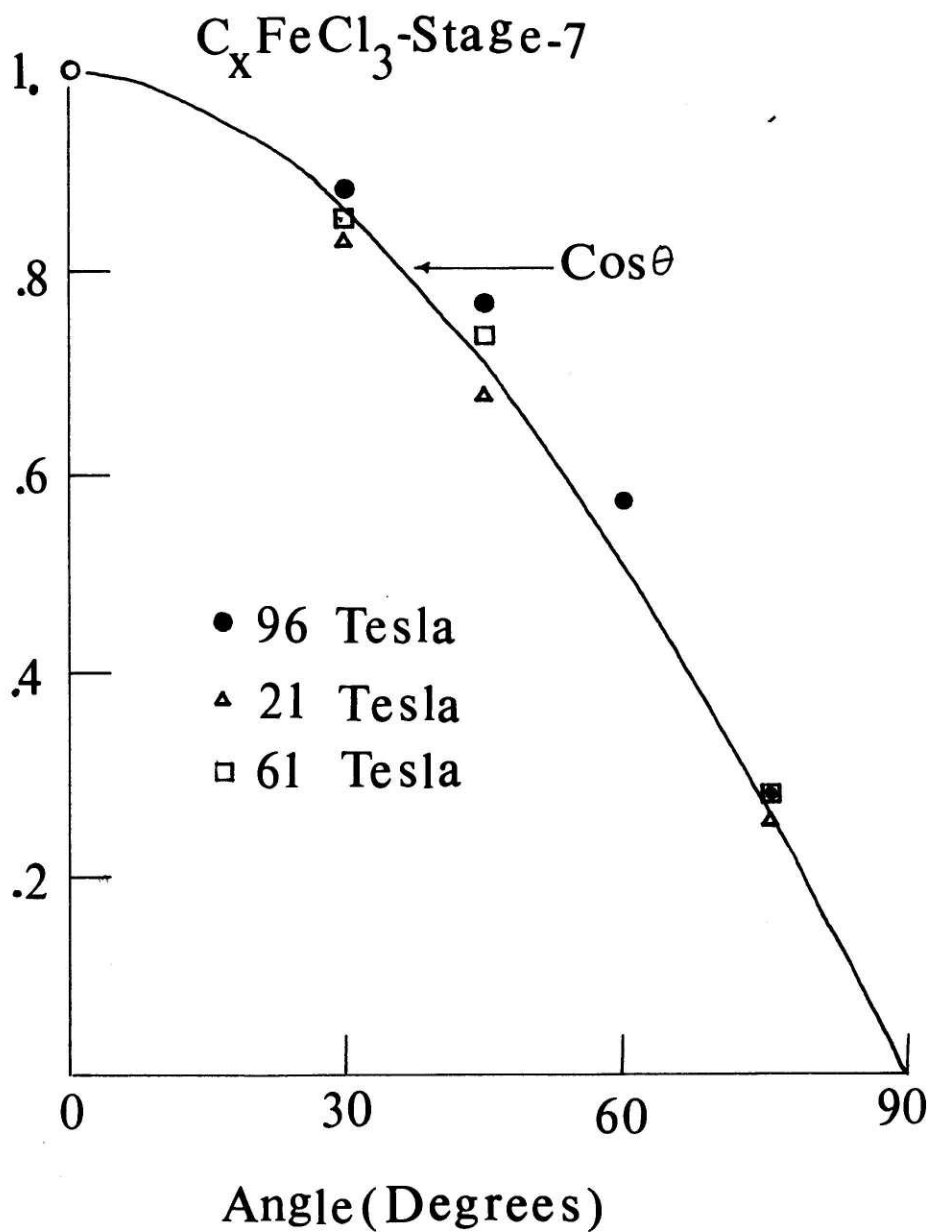
Figure 4.5: $\nu(0)/\nu(\theta)$ vs. Angle for C_xFeCl_3 - Stage 7.
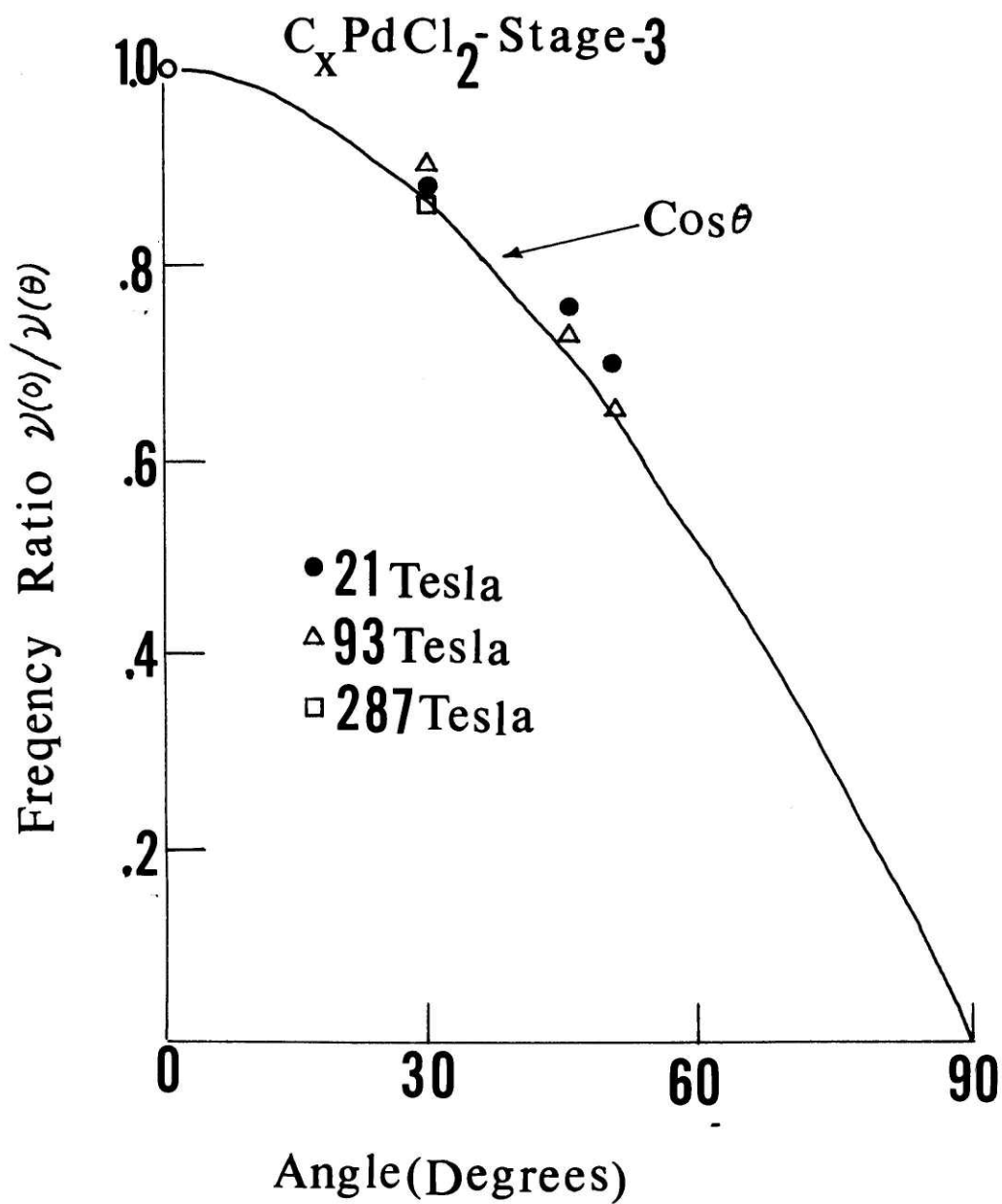
Figure 4.6: $\nu(0)/\nu(\theta)$ vs. Angle for C_xPdCl_2 - Stage 3.
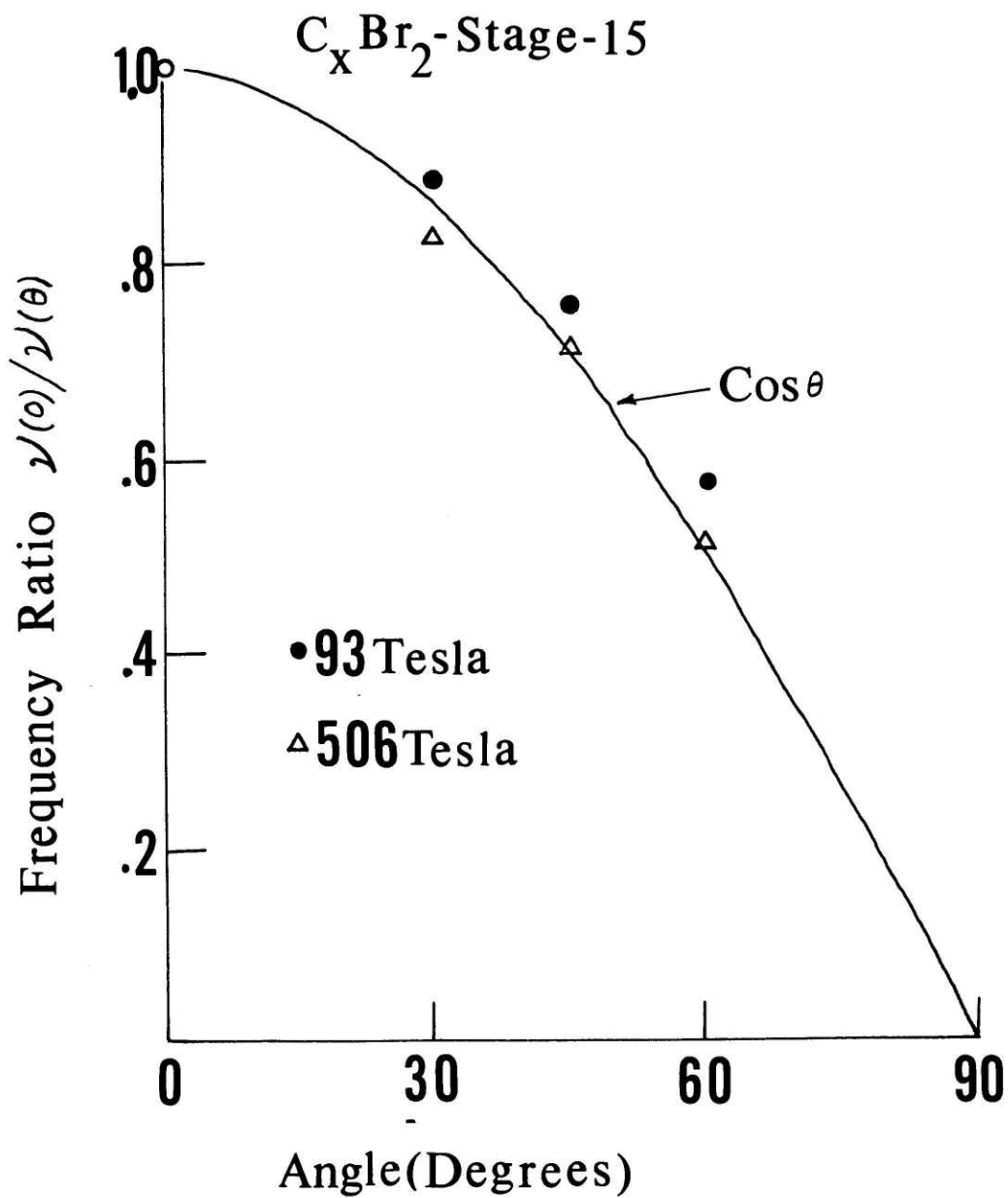
Figure 4.7: $\nu(0)/\nu(\theta)$ vs. Angle for C_xBr_2 - Stage 15.
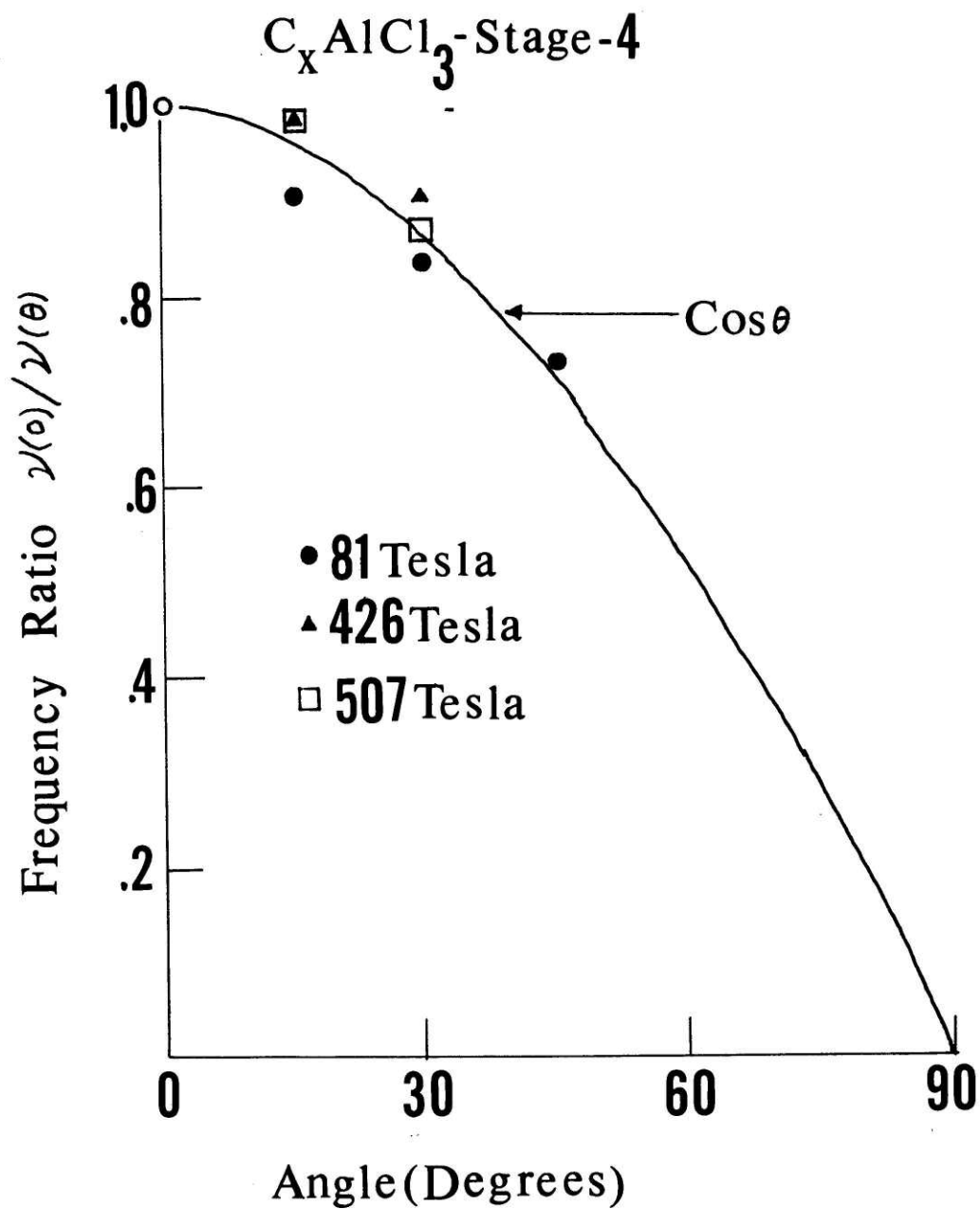
Figure 4.8: $\nu(0)/\nu(\theta)$ vs. Angle for C_xAlCl_3 - Stage 4.
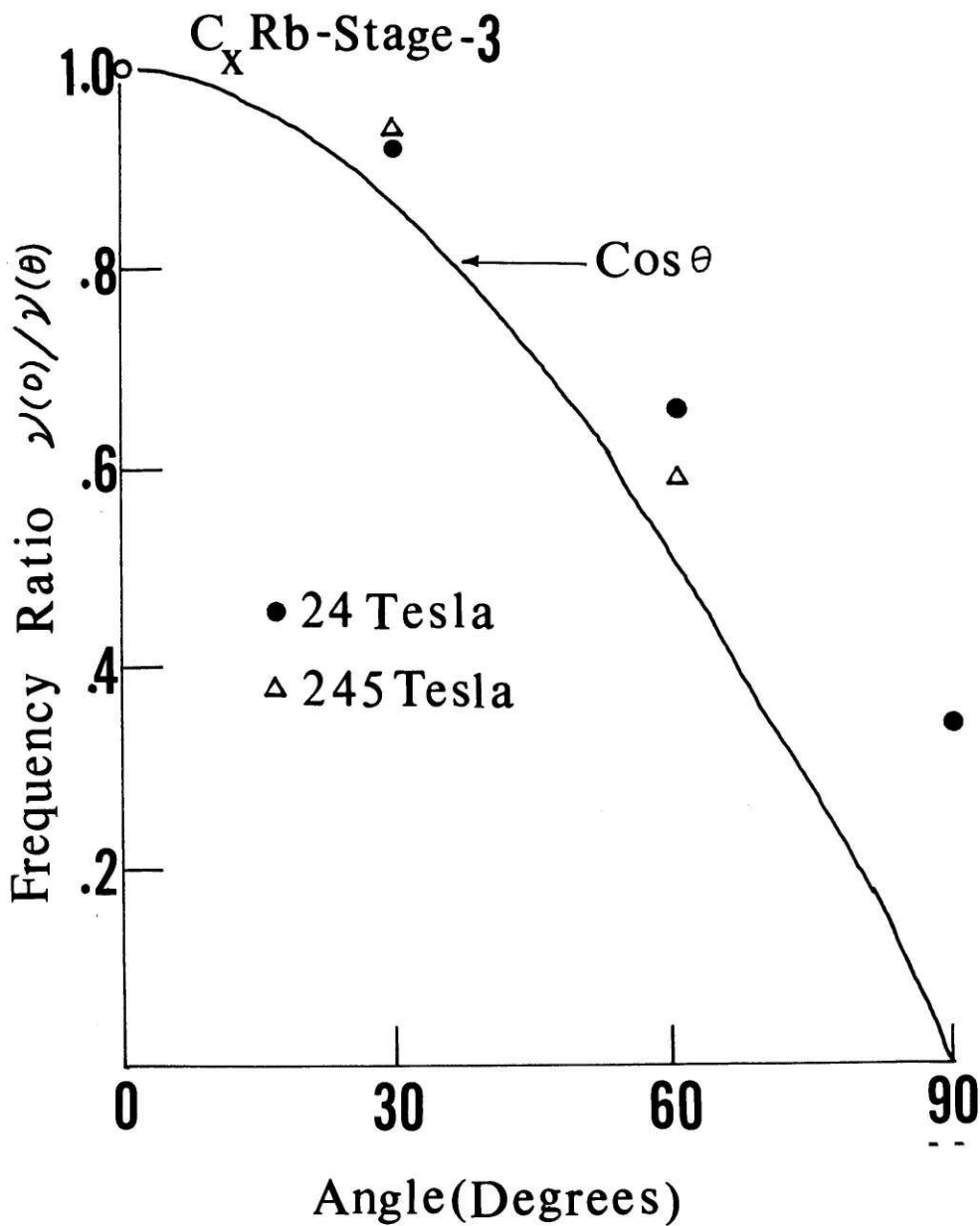
Figure 4.9: $\nu(0)/\nu(\theta)$ vs. Angle for $C_x Rb$ - Stage 3.

oscillations and those frequencies which do not disappear as the sample
is rotated. In addition to the major peaks in the power spectrum,
there are a host of smaller peaks observed in the spectrum of the
above compounds which are ommited in the tables. The angular accuracy
of all data is ±2° and the accuracy in the frequencies is ±5 Tesla.
The angular dependence of frequencies observed in C_xFeCl_3 (stage 1,
3, and 7) are shown in the figures 4.3, 4.4, and 4.5 respectively. A
cylindrical Fermi surface has a cosine dependence for $\frac{\nu(0)}{\nu(\theta)}$ and this
cosine dependence is drawn in the figures as a reference. The low
frequency 20 Tesla shows identical behavior in both stages 2 and 7
compounds and has an anisotropy between $\theta = 0$ and 90° of about 2. Larger
frequencies exhibit more cosine-like behavior. The estimates of
anisotropy are found in the next chapter.

Table 4.4 shows the frequencies obtained as a result of
Shubnikov-de Haas measurements on three samples of C_xPdCl_2 (stage 3).
The angular dependence of the 92 T, 402 T, and 504 T frequencies for
sample 2 are shown in figure 4.6. From table 4.4 and figure 4.6 one
notes some variation of frequencies for samples of the same nominal
compound (C_xPdCl_2 stage 3).

Tables 4.5 and 4.6 contain frequencies as a function of angle
for a dilute C_xBr_2 compound (corresponding approximately to stage 5)
and C_xAlCl_3 (stage 4). The angular dependences are plotted in figures
4.7 and 4.8, respectively.

All the materials considered so far had acceptors as intercalants;
however C_xRb is an example of a donor intercalation compound. Results

TABLE 4.1

Shubnikov-de Haas Frequencies (in Tesla)

As A Function of Angle for C_xFeCl_3 - Stage 1

$\theta = 0$	$\theta = 30°$	$\theta = 60°$	$\theta = 70°$	$\theta = 90°$
21	24	33	36	44
93	102	160	247	-
287	329	513	816	-
599	-	-	-	-

TABLE 4.2

Shubnikov-de Haas Frequencies (in Tesla)

As A Function of Angle for C_xFeCl_3 - Stage 3

$\theta = 0$	$\theta = 30°$	$\theta = 45°$	$\theta = 60°$	$\theta = 90°$
20	23	27	32	45
102	117	144	187	-
540	623	761	1072	-

TABLE 4.3

Shubnikov-de Haas Frequencies (in Tesla)

As A Function of Angle for $C_X FeCl_3$ - Stage 7

$\theta = 0$	$\theta = 30°$	$\theta = 45°$	$\theta = 60°$	$\theta = 75°$	$\theta = 90°$
90	103	116	161	260	-
210	250	310	Excessive Noise	780	-
610	720	820	Excessive Noise	2300	-

TABLE 4.4

Sample Dependence of SdH Frequencies

for 3-Samples of $C_X PdCl_2$

Sample-1	Sample-2	Sample-3	$\mu \pm \sigma$	$\frac{\sigma}{\mu}$ x 100
75	64	66	68 ± 5	7%
102	92	100	98 ± 4	4%
372	371	375	372 ± 2	5%
437	402	429	423 ± 15	4%
504	495	499	499 ± 3	2%

TABLE 4.5

Shubnikov-de Haas Frequencies (in Tesla)

As A Function of Angle for C_xBr2 - Stage 15

$\theta = 0$	$\theta = 30°$	$\theta = 45°$	$\theta = 60°$
93	106	123	166
506	610	707	1005

TABLE 4.6

Shubnikov-de Haas Frequencies (in Tesla)

As A Function of Angle for C_xAlCl_3 - Stage 4

$\theta = 0$	$\theta = 15°$	$\theta = 30°$	$\theta = 45°$
81	90	96	113
426	438	472	-
507	519	593	-

for the frequencies and angular dependence are shown in table 4.7 and figure 4.9, respectively.

Table 4.8 shows the frequencies observed for zero angle for C_xFeCl_3 stages 1, 3 and 7. The amplitudes for each stage are in arbitrary units and the amplitudes are scaled so that the maximum amplitude within each stage is 1,000 (harmonics are excluded in table 4.8). Some of these frequencies were omitted in tables 4.1 to 4.3 since they disappear quickly as the sample is rotated even as low as 15°.

Table 4.9 summarizes the main frequencies observed for all compounds at zero angle.

4.2. Perspective

All acceptor compounds studied have a "large" frequency in the range 500 to 600 Tesla. It appears that in all the compounds studied, larger frequencies exhibit more anisotropy than smaller frequencies. In particular, frequencies of order 500 tesla follow the cosine curve quite closely.

The effect of periodicity (staging) in the c-direction can be modelled by introducing cuts into the ellipsoidal Fermi surface as shown in the figure 2.6. Simple calculations show that areas of the cuts in the ellipsoid obey the following relation.

$$S(n) = S_o - \pi \left(\frac{2\pi}{I_c}\right)^2 \left(\frac{m_x}{m_z}\right) n^2 \qquad (4.1)$$

TABLE 4.7

Shubnikov-de Haas Frequencies (in Tesla)

As A Function of Angle for C_xRb - Stage 3

$\theta = 0$	$\theta = 30°$	$\theta = 60°$	$\theta = 70°$
24	26	36	72
245	260	410	-

TABLE 4.8

Shubnikov-de Haas Frequencies (in Tesla) of C_xFeCl_3 Systems

Stage-1	Stage-3	Stage-7
21 (576)	20 (424)	very weak
93 (1000)	87 (283) 102 (264)	90 (1000)
132^T(529)	149 (311)	very weak
202 (223)	200 (302)	210 (491)
287 (412)	288 (151)	280 (113)
435 (256)	457 (311)	430 (130)
560 (94)	540 (1000) 560 (821)	520 (373)
599 (229)	617 (585)	610 (876)

Quantities in the parenthesis are relative amplitudes for each stage and the amplitudes are scaled so that the maximum amplitude with each stage is 1000 (harmonics are excluded).

TABLE 4.9

Main Shunikov-de Haas Frequencies (in Tesla)

For All Materials Studied

C_xFeCl_3 Stage-1	C_xFeCl_3 Stage-3	C_xFeCl_3 Stage-7	C_xPdCl_2 Stage-3	C_xBr_2 Stage-15	C_xAlCl_3 Stage-4	C_xRb Stage-3
21	20	-	-	-	-	24
93	102	90	98	93	81	-
202	200	210	-	-	-	245
435	457	430	423	-	426	-
560	540	520	499	506	507	-
599	617	610	Weak 595 606	Weak 620	-	-

Thus the plot of the appropriate frequencies versus n^2 produces a straight line in which the slope determines the anisotropy of the ellipsoid. Figure 4.10 shows the fit for the peaks in the power spectrum of C_xFeCl_3 - Stage 7. The figure shows that various peaks (ignoring their amplitudes) fall into a well defined group if the lines are extrapolated into negative frequencies. The extrapolation to the negative frequencies may be an indication of the joining of two adjacent ellipsoids belonging to different Brillouin zones as indicated in figure 4.11.

From the slopes of these lines one can estimate the anisotropy of the ellipsoid. In particular, one estimates from the slope of the line containing the 90 Tesla frequency an anisotropy of 16.5 which seemingly is in conflict with the previously obtained anisotropy of 2 from figure 4.3. The conflict is resolved if one takes the 880 tesla frequency (figure 4.10) as the belly of the ellipsoid rather than the 90 tesla frequency, as indicated in the figure 4.12. The 20 tesla frequency could not be fit into any groups.

The frequencies obtained in other compounds fall into groups similar to C_xFeCl_3 - stage 7, giving more support for introduction of cats in the ellipsoidal Fermi surface as a result of staging. One should note that the resolution of the analyzed power spectrum is not good enough to fit large anisotropy (large frequency) cross section. As a result, the idea of the sliced ellipsoidal Fermi surface remains a suggestion (conjesture) for further research.

$$\mathcal{V} = \mathcal{V}_0 - \alpha n^2$$

C$_x$FeCl$_3$-Stage-7

$\mathcal{V}(\theta=0)$ In 100 Tesla
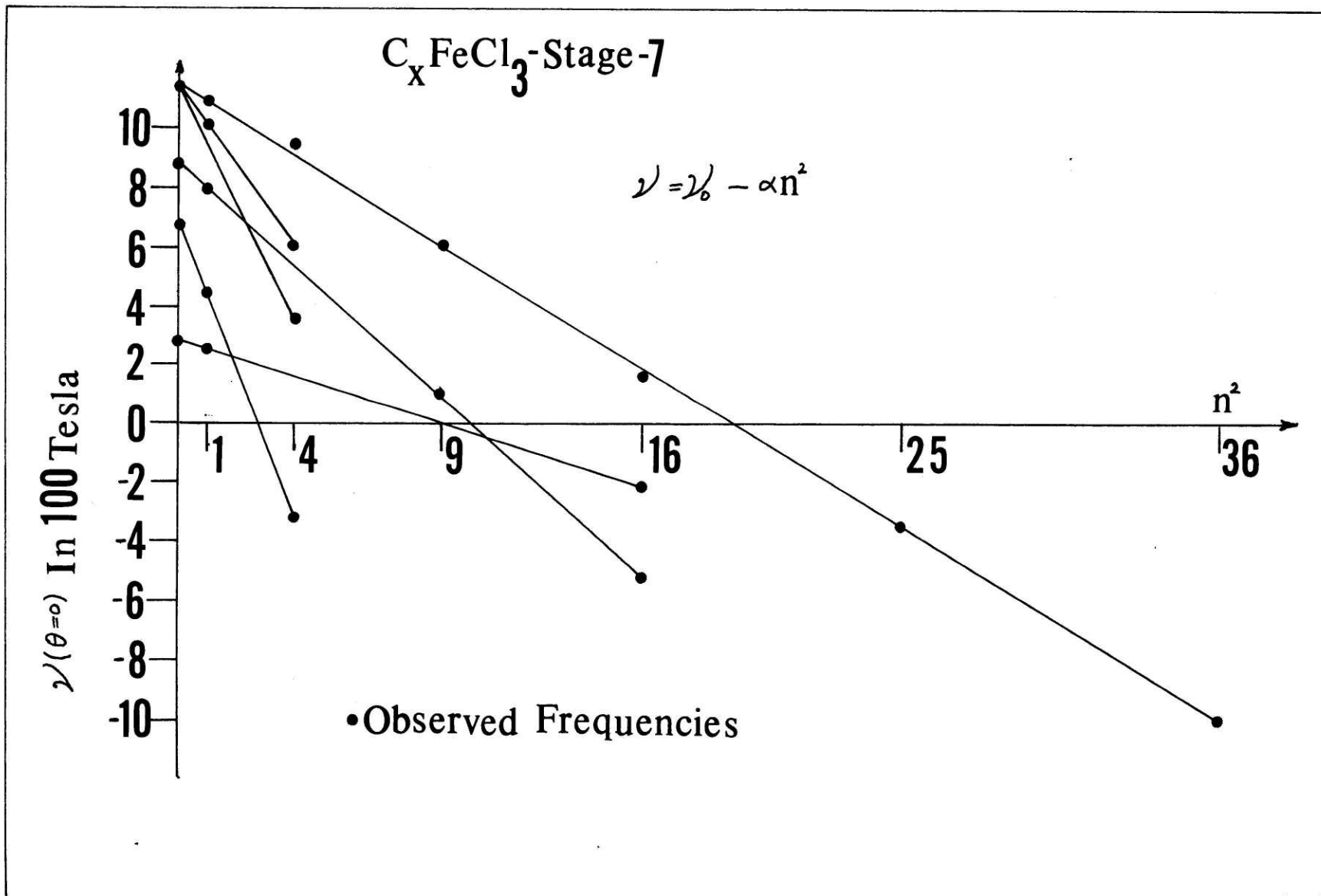
• Observed Frequencies

Figure 4.10: Attempted Fit of Maxima to the Sliced Ellipsoidal Model
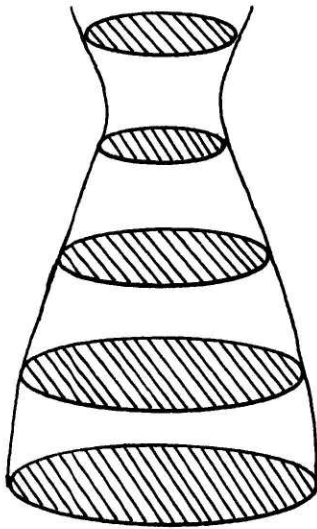
(C$_x$FeCl$_3$ - Stage 7).

Figure 4.11:   Joining of Two Adjacent Ellipsoidal Fermi
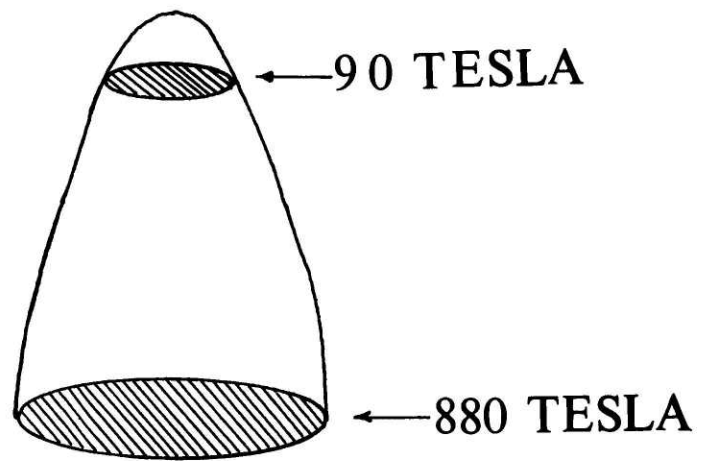
Surfaces.

Figure 4.12:   Identification of Two Observed Frequencies
as the Cuts in an Ellipsoidal Fermi Surface.

CHAPTER 5

CONCLUSION

Section 5.1 of this chapter discusses the shapes of the Fermi
surfaces of donor and acceptor graphite intercalation compounds.
Section 5.2 comments on the sample dependence of the observed frequencies.
The stage and intercalant dependence of frequencies are discussed in
sections 5.3 and 5.4, respectively. Finally, section 5.5 contains
general conclusions and comments for further studies.

5.1. The Shape of the Fermi Surfaces

The results of angular dependence of the frequencies are shown
in figures 4.3, 4.4, 4.5, 4.6, 4.7, 4.8 and 4.9. One can note two
general features from these figures. The anisotropy of the ellipsoids
increases as the magnitude of the frequencies increases. This feature
is independent of the intercalant species and stage. All large
frequencies (greater than 300 Tesla) follow the cosine-law behavior
closely. Furthermore, the angular dependence of the large frequencies
follows a cosine law more closely as the angle is increased. This
suggests that anisotropy estimates of the surfaces are more sensitive
to the values of the large angle frequencies. Therefore, the data
available at the largest angle are used to estimate the anisotropy
of the ellipsoidal Fermi surfaces. For the ellipsoid $\frac{k_x^2 + k_y^2}{m_x} + \frac{k_y^2}{m_z} = E$,

the following formula is used to estimate the anisotropy of the Fermi surfaces

$$\varepsilon = \sqrt{\frac{\overline{m_z}}{m_x}} = \left[\frac{\sum\limits_i \sin^4\theta_i}{\sum\limits_i \sin^2\theta_i \left\{ \left| \frac{\nu(0)}{\nu(\theta)} \right|^2 - \cos^2\theta_i \right\}} \right]^{1/2}$$

(derivation in Appendix I).

The Table 5.1 lists the anisotropy estimates for the compounds that were studied.

The slicing of ellipsoidal Fermi surfaces are promising as providing a possible model for the dilute compounds ($n \geq 5$). This model was particularly successful in the case of $C_x FeCl_3$ (stage 7) as is illustrated in figure 4.10. The slopes of the lines in the figure can be used to estimate the anisotropy of the ellipsoidal Fermi surfaces. As was computed in the previous chapter, the following relation (Eq. (4.1) holds between the anisotropy and the slope of the lines.

$$S = S_0 - \pi \left(\frac{2\pi}{I_0} \right)^2 \left(\frac{m_x}{m_z} \right) n^2 \qquad (4.1)$$

where $I_c \equiv$ distance between two adjacent intercalant layers.

$$|slope| = \pi \left(\frac{2\pi}{I_0} \right)^2 \frac{1}{\varepsilon^2} \; ; \qquad \varepsilon = \sqrt{\frac{\overline{m_z}}{m_x}} \; ;$$

$I_0 = 29.51$ A° for $C_x FeCl_3$ - stage 7.

Estimates of the anisotropies are summarized in the table 5.2. There is no estimate for the 210 Tesla SdH frequency in table 5.2, Since it could not be fit into any groups of frequencies. As far as the 90 Tesla frequency in C_xFeCl_3 (stage 7) is concerned, there is qualitative agreement for the anisotropy estimate between the above value (ε = 4.06 from table 5.2) and the previously obtained value from angular studies (ε = 4.2, from table 5.1). However, there is no such agreement fro the 610 Tesla frequency. This could be due to incorrect group fitting of the 610 Tesla frequency (fig. 4.11). One notes that the sliced ellipsoidal Fermi surface model is consistent with the observation of an increase in the anisotropy with increasing frequencies. One would expect possible warping in the ellipsoidal Fermi surfaces of the graphite intercalation compounds on the basis of the appearance of harmonics of the observed frequencies in the power spectra of the Shubnikov-de Haas oscillations. Thus, the expected shapes of the Fermi surfaces are long ellipsoids along the c-axis with possible warping.

5.2. Sample Dependence of the Frequencies

Variations in frequencies within samples of the same intercalant and stage provides an estimate for the accuracy of the reported data. Table 4.4 shows the variation in the Shubnikov-de Haas frequencies of C_xPdCl_2 of stage-3. The typical variation in frequency is taken as 4%.

TABLE 5.1

Anisotropies of the Frequencies (Tesla)

C_xFeCl_3 - Stage 1

21	$\varepsilon = 2.1 \pm .4$
93	$\varepsilon = 6.0 \pm 1.5$
287	$\varepsilon = 11.5 \pm 3$

C_xFeCl_3 - Stage 3

21	$\varepsilon = 2.3 \pm .5$
102	$\varepsilon = 4 \pm 1.5$
540	$\varepsilon = 15 \pm 2.5$

C_xFeCl_3 - Stage 7

90	$\varepsilon = 4.2 \pm 1.5$
210	$\varepsilon = 13.0 \pm 2.5$
610	$\varepsilon = 16.7 \pm 3.5$

C_xBr_2 - Stage 15

| 93 | $\varepsilon = 3.4 \pm 1.5$ |
| 506 | $\varepsilon = 14.5 \pm 4$ |

C_xAlCl_3 - Stage 4

| 81 | $\varepsilon = 6.0 \pm 1.5$ |
| 426 | $\varepsilon = -$ |

C_xRb - Stage 3

| 24 | $\varepsilon = 3.0 \pm .5$ |
| 245 | $\varepsilon = 4.4 \pm 1.5$ |

TABLE 5.2

Anisotropies of C_xFeCl_3 - Stage 7 Frequencies (Tesla)

Estimated From the Slopes of the Lines in Fig. 4.11

90	$\varepsilon = 4.06$
210	$\varepsilon = -$
610	$\varepsilon = 4.96$

5.3. Stage Dependence of the Frequencies

The stage dependence of the frequencies were studied on C_xFeCl_3 for stages 1, 3 and 7. Table 4.8 lists the frequencies of C_xFeCl_3 (zero angle) for the above three stages. The measured data is insufficient to determine any stage dependence of the frequencies. In order to obtain the stage dependence of frequencies, each frequency should be accompanied by its corresponding effective mass. Variation of the frequency as a function of stage for each effective mass yields the stage dependence of each frequency. An effective mass determination involves temperature dependent measurements of Shubnikov-de Haas oscillations.

5.4. Intercalant Dependence of the Frequencies

Table 5.3 lists all the zero angle frequencies observed for the compounds that were studied. In order to correlate the listed data (i.e. intercalant dependence of frequencies), one has to appeal to some theoretical model (band calculations, etc.) for graphite intercalation compounds which is unavailable at the moment. In the case of the donor compound C_xRb (stage 3) there are only two dominant frequencies as opposed to many frequencies in the acceptor compounds (zero angle). This sample feature of the donor compound makes it an ideal system for detailed study of graphite intercalation compounds.

TABLE 5.3

Zero Angle Frequencies Observed in All Studered Graphite Intercalation Compounds

FeCl$_3$-Stage-1	FeCl$_3$-Stage-3	FeCl$_3$-Stage-7	PdCl$_2$-Stage-3	Br$_2$-Stage-15	AlCl$_3$-Stage-4	Rb-Stage-3
21	20	-	-	-	-	24
93	102	90	75 102	93	81	
287	-	210	372 437	-	426	245
599	540	610	504	506	507	

5.5. Conclusions and Comments

Possible shapes of the Fermi surfaces for graphite intercalation compounds are sliced ellipsoids formed by zone folding of a graphite like constant energy surface along the c-axis, with possible warping similar to that of pure graphite. The ellipsoidal Fermi surfaces for acceptor compounds have large cross sectional areas perpendicular to the c-axis (880 Tesla in $FeCl_3$-stage 7 at the maxima, fig. 4.12) and an anisotropy of greater than 16 obtained from the angular dependence of the Shubnikov-de Haas oscillations. The donor compound C_xRb shows lower anisotropy namely about 3 for the ellipsoidal Fermi surface.

In figure 4.10 the lines are extrapolated to negative frequencies. A possible interpretation of the negative frequencies could be the joining of two pieces of ellipsoidal Fermi surface as is illustrated in figure 4.11. However, to check the slicing model one needs more resolution on the power spectra and improved data analysis on a variety of graphite intercalation compounds. Therefore, the slicing model remains a suggestion for further research.

Since the ellipsoidal Fermi surfaces are highly anisotropic in acceptor compounds, large angle measurements of Shubnikov-de Haas frequencies (in particular from 75° to 90°) are essential for determining the anisotropy of the Fermi surfaces.

An improvement is possible in the geometry of the sample in the magnetic field as shown in figure 3.1. At $\theta = 0$, one is measuring the transverse magnetoresistance, whereas at $\theta = 90°$, the measurements correspond to the longitudinal magnetoresistance. For any angle
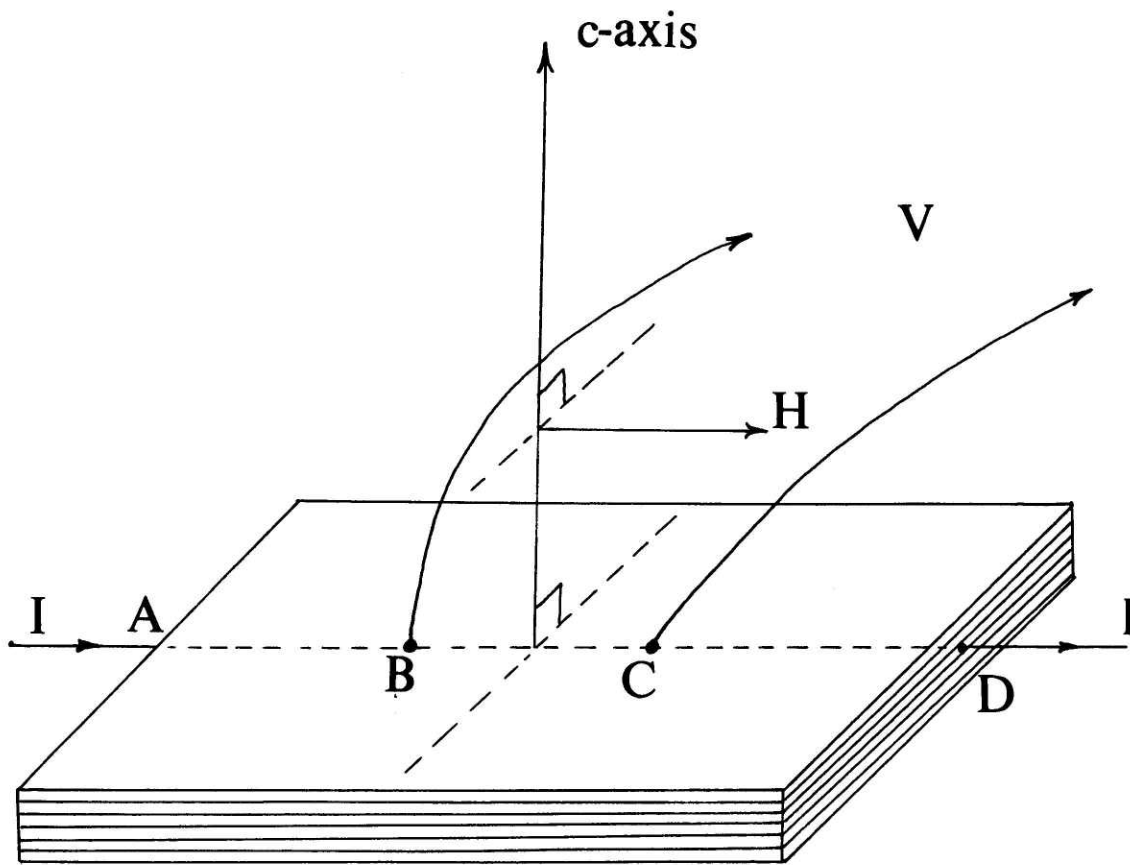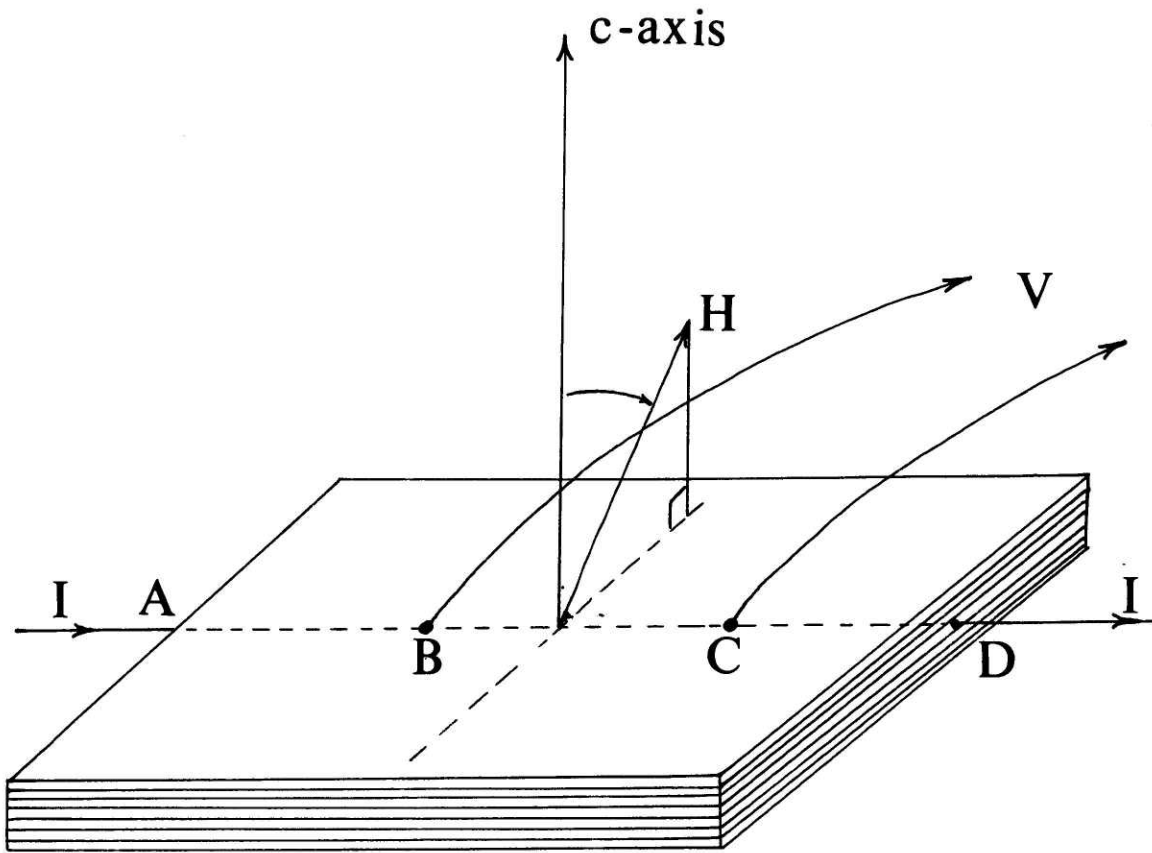
Figure 5.1: Longitudinal Magnetoresistance

Figure 5.2:   Transverse Magnetoresistance

between zero and 90°, there would be a mixed configuration. An
expression for the contribution of ith carrier to the magnetoresistance
(as explained in the previous chapter) is

$$\rho_i = H^{\ell_i} \sum_{r=1}^{\infty} B(r) \frac{rU_i}{\sinh rU_i} \exp\left(-\frac{rU_i T_D}{T}\right) \cos\left(\frac{rehA}{eH} - \phi_i(r)\right)$$

where

$$U_i = \frac{2\pi^2 kT}{h\omega_i} \;.$$

In general, ℓ_i, B, and T_D are different for the transverse and
longitudinal cases. Therefore, the transverse and longitudinal
magnetoresistance should be measured separately if one is interested
in ℓ_i and T_D which contain information on the mechanism of electron
scattering and the magnitude of energy level broadening, respectively.
The modified geometries are illustrated in figures 5.1 and 5.2 for
longitudinal and transverse configurations, respectively.

Data reduction should be improved also. Since the RS1 program
could only accommodate 1024 points for computation of the power spectra,
there is a trade-off between the resolution of the frequencies and
the maximum frequencies deduced from the data. This limitation is
surmountable by using a program capable of handling more points for
computation of power spectra.

With the help of band calculations for graphite intercalation
compounds, one could attempt a more detailed analysis of the
Shubnikov-de Haas frequencies.

A possible extension of the present project is to study the temperature dependence of the Shubnikov-de Haas frequencies which provides direct information on the values of the effective masses. The effect of pressure is to increase the electronic interaction between layers of graphite and intercalant. Thus, one can obtain information on the nature of interaction between layers by studying the pressure dependence of the Shubnikov-de Haas frequencies.

REFERENCES

1. P.N. Argyres, J. Phys. Chem. Solids, Vol. 4, pp. 19-26, 1958.

2. E.M. Lifshits and A.M. Kosevich, J. Phys. Chem. Solids, Vol. 4 pp. 1-10, 1958.

3. E.M. Lifshits, J. Phys. Chem. Solids, Vol. 4, pp. 11-18, 1958.

4. E.N. Adams and T.D. Holstein, J. Phys. Chem. Solids, Vol. 10, pp. 254-276, 1959.

5. M.S. Dresselhaus, G. Dresselhaus, J.E. Fisher, Phys. Rev. B, Vol. 15, No. 6, 15 March 1977.

6. A.S. Bender and D.A. Young, J. Phys. C. Solid State Phys., Vol. 5, 1972.

7. J. Bok, Proceedings of the International Conference on High Magnetic Fields, in Semiconductors, Oxford, Sept. 1978.

8. G. Landwehr, Physics of Solids in Intense Magnetic Fields, Chapter 22, E.D. Haidemnakis, ed.

9. W. Zawadzki, Physics of Solids in Intense Magnetic Fields, Chapter 13, E.D. Haidemnakis, ed.

10. L. Onsager, Phil. Mag. 43, 1006, 1952.

APPENDIX I

DERIVATION OF ANISOTROPY ESTIMATION FORMULA

A simple calculation shows that for the ellipsoid $\dfrac{k_x^2+k_y^2}{m_x} + \dfrac{k_z^2}{m_z} = E$ the following resolution holds for $v(0)$ and $v(\theta)$ (cross sections at zero and θ angle, respectively) as shown in the figure.

$$\frac{v(0)}{v(\theta)} = \sqrt{\cos^2\theta + \frac{1}{\epsilon^2}\sin^2\theta} \quad \text{where } \epsilon^2 \equiv \frac{m_z}{m_x}$$

Defining

$$x^2 \equiv \sum_i \left[\cos^2\theta_i + \frac{1}{\epsilon^2}\sin^2\theta_i - \frac{v^2(0)}{v^2(\theta_i)}\right]^2$$

and minimizing it with respect to $\dfrac{1}{\epsilon^2}$

$$\frac{\partial x^2}{\partial\left(\dfrac{1}{\epsilon^2}\right)} = 2\sum_i \sin^2\theta_i\left(\cos^2\theta_i + \frac{1}{\epsilon^2}\sin^2\theta_i - \frac{v^2(0)}{v^2(\theta_i)}\right) = 0$$

results the estimate for the anisotropy ϵ which is:

$$\epsilon = \left[\frac{\sum_i \sin^4\theta_i}{\sum_i \sin^2\theta_i\left(\left\{\dfrac{v(0)}{v(\theta_i)}\right\}^2 - \cos^2\theta_i\right)}\right]^{1/2}$$
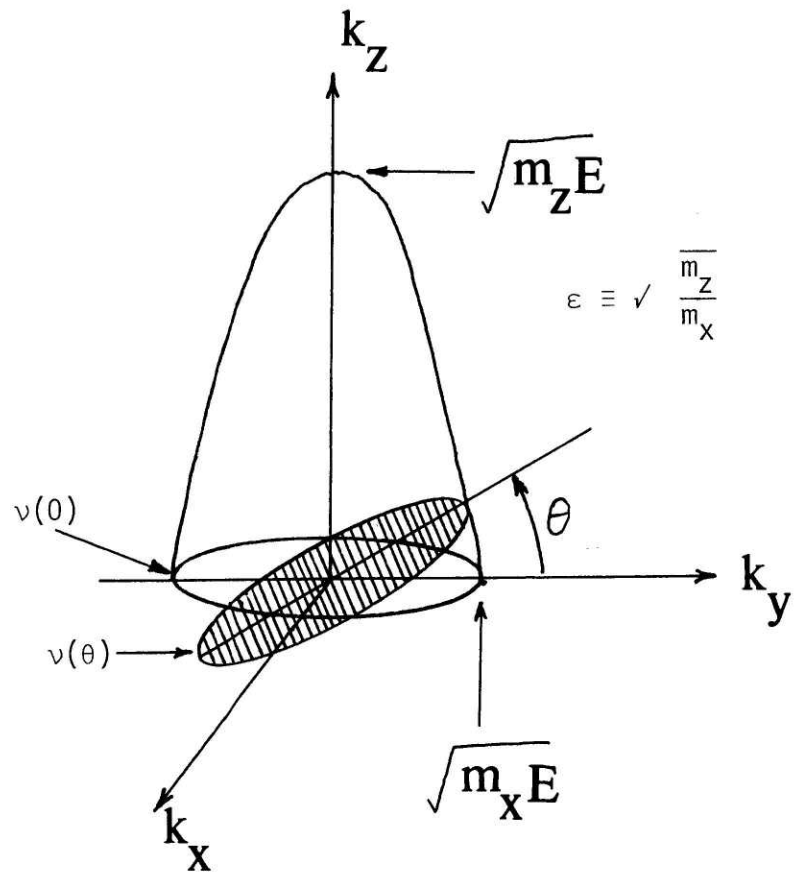
Figure A.1: Cross Sections $\nu(\theta)$ and $\nu(0)$